

Phase coexistence at the first-order Mott-transition revealed by pressure-dependent dielectric spectroscopy of κ -(BEDT-TTF)₂Cu₂(CN)₃

R. Rösslhuber,¹ A. Pustogow,¹ E. Uykur,¹ A. Böhme,¹ A. Löhle,¹
R. Hübner,² J. Schlueter,³ Y. Tan,⁴ V. Dobrosavljević,⁴ and M. Dressel¹

¹*1. Physikalisches Institut, Universität Stuttgart, Pfaffenwaldring 57, 70569 Stuttgart, Germany*

²*Inst. Functional Matter and Quantum Techn., Universität Stuttgart, Pfaffenwaldring 57, 70569 Stuttgart, Germany*

³*Material Science Division, Argonne National Laboratory, Argonne, Illinois 60439-4831 and
National Science Foundation, Alexandria, Virginia 2223, U.S.A.*

⁴*National High Magnetic Field Laboratory, Florida State University, Tallahassee, U.S.A.*

(Dated: November 18, 2021)

The dimer Mott insulator κ -(BEDT-TTF)₂Cu₂(CN)₃ can be tuned into a metallic and superconducting state upon applying pressure of 1.5 kbar and more. We have performed dielectric spectroscopy measurements (7 kHz to 5 MHz) on κ -(BEDT-TTF)₂Cu₂(CN)₃ as a function of temperature (down to $T = 8$ K) and pressure (up to $p = 4$ kbar). At ambient conditions, a relaxor-like dielectric behavior develops below 50 K that shifts toward lower temperatures as the crystal is pressurized. Interestingly, a second peak emerges in $\epsilon_1(T)$ around $T = 15$ K, which becomes strongly enhanced with pressure and is attributed to a small volume fraction of metallic puddles in the insulating host phase. When approaching the phase boundary, this peak diverges rapidly reaching $\epsilon_1 \approx 10^5$. Our dynamical mean-field theory calculations substantiate that the dielectric catastrophe at the Mott transition is not caused by closing the energy gap, but due to the spatial coexistence of correlated metallic and insulating regions. We discuss the percolative nature of the first-order Mott insulator-to-metal transition in all details.

PACS numbers: 71.30.+h, 74.70.Kn, 72.90.+y, 77.22.-d

I. INTRODUCTION AND MOTIVATION

The quasi two-dimensional organic charge-transfer salts (BEDT-TTF)₂X became model compounds for investigating the interplay of strongly correlated electrons, reduced dimensionality, spin-charge interactions and ordering phenomena¹⁻³. Their molecular composition enables the fine-tuning of physical properties by modifying the donor molecules bis-(ethylenedithio)-tetrathiafulvalene (BEDT-TTF), varying the monovalent anions X, or by applying comparably low pressures – usually a few kbar are sufficient to induce drastic changes⁴. The dimerized κ -phase compounds have been established as prime examples for the bandwidth-tuned Mott insulator-metal transition (IMT) and the quantum critical region above⁵⁻¹⁰.

For the last decade, the dimer Mott insulator κ -(BEDT-TTF)₂Cu₂(CN)₃ attracted most attention as it is considered the prime candidate for a quantum spin liquid^{11,12}. The nature of this highly degenerate spin state and its exotic spin excitations are subject of intense studies and controversial discussions^{13,14}. The absence of long-range magnetic order even at lowest temperatures provides the opportunity to investigate the genuine Mott transition^{8,9,15}, which is solely driven by Coulomb interactions, without breaking any symmetry. Nevertheless, recent studies revealed that for these layered BEDT-TTF compounds the lattice properties play an important role – in addition to disorder – and the interaction with the anions can be decisive¹⁶⁻¹⁸.

Besides these fundamental issues, there are some more peculiarities observed in κ -(BEDT-TTF)₂Cu₂(CN)₃,

which are far from being understood. Around $T \approx 6$ K the thermal expansion exhibits a pronounced anomaly¹⁹ with related features observed in specific heat²⁰, thermal conductivity²¹, ultrasound propagation²², magnetic susceptibility²³, and microwave dielectric properties²⁴. Furthermore, a relaxor-type ferroelectric response was observed in the audio- and radio-frequency range below $T \approx 50$ K^{25,26}. Previous attempts to link it to charge disproportionation within the dimers due to intersite Coulomb repulsion, dubbed quantum electric dipole or paired-electron crystal²⁷⁻³⁰, could not be verified in experiment as various spectroscopic methods have unambiguously proven homogeneous charge distribution on the molecules³¹⁻³⁶.

In order to motivate our detailed experimental investigations and analysis, theoretical calculations and discussions, let us first give an overview on the temperature-dependent dielectric response of κ -(BEDT-TTF)₂Cu₂(CN)₃ in the various regimes. In Fig. 1 we plot the real part of the dielectric permittivity $\epsilon_1(T)$ for selected frequencies and pressures as indicated. Starting from ambient conditions, a pronounced peak dominates the temperature dependence of the dielectric constant. The maximum shifts to lower temperatures as pressure increases [Fig. 1 (a-e)] and, exceeding $p = 1.22$ kbar, it moves out of the accessible temperature window. Most important, however, are the drastic changes of the dielectric response around the insulator-to-metal transition at $p_{\text{IMT}} = 1.45$ kbar⁸. For $p = 1.45$ up to 2.2 kbar, ϵ_1 is strongly enhanced for $T < 20$ K with a frequency-dependent amplitude even exceeding 10^5 at $f = 7.5$ kHz [Fig. 1(f-h)]. As pressure increases further, the onset

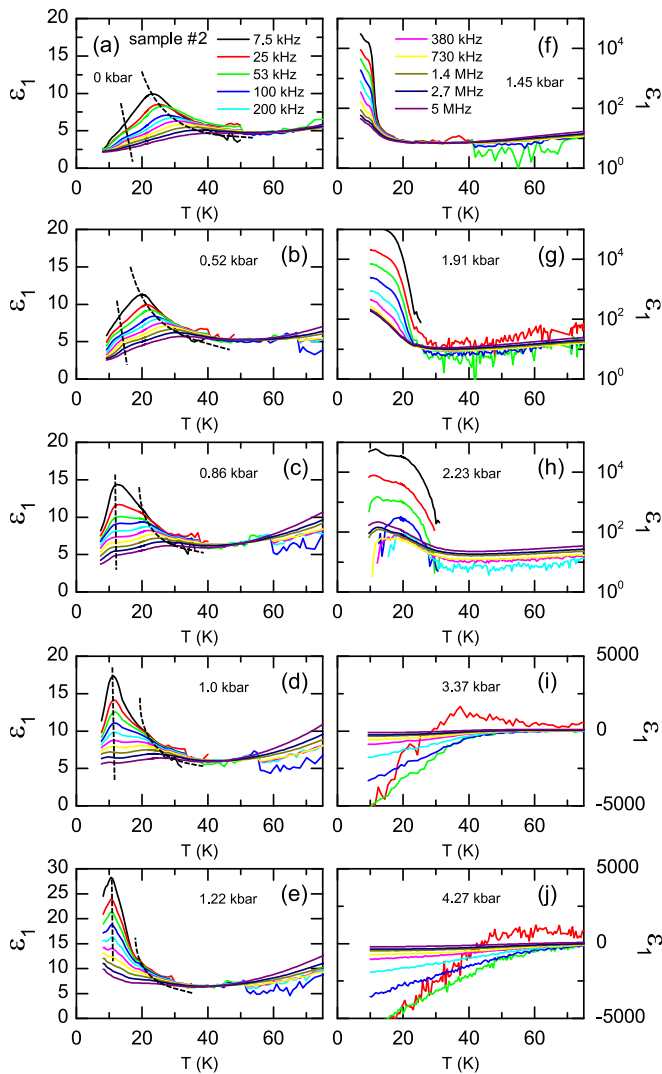


FIG. 1. Plot of the dielectric permittivity $\varepsilon_1(T)$ of κ -(BEDT-TTF) $_2$ Cu $_2$ (CN) $_3$ for several frequencies upon increasing pressure. Note the different ordinates used in the various panels. (a) At $p = 0$ kbar and below $T = 50$ K, we observe a relaxor-type ferroelectric peak with shrinking amplitude that shifts to higher temperature with increasing frequency. (b-e) Additionally, a shoulder-like feature is revealed at ambient pressure around $T = 15$ K which develops into a second peak upon pressurizing. (f-h) In the coexistence phase between $p = 1.45$ and 2.23 kbar, an enormous increase of ε_1 is observed which is strongly frequency-dependent and attributed to spatially separated metallic and insulating regions. (i,j) Above $p = 3.37$ kbar, $\varepsilon_1 < 0$ for nearly all measured frequencies indicating metallic behavior.

of the dielectric anomaly shifts to higher temperatures, reaching about 30 K at $p = 2.23$ kbar, for instance [Fig. 1(h)]. We ascribe this observation to a coexistence region centered around the Mott IMT, where spatially segregated metallic regions in an insulating matrix grow in a percolative manner. At $p = 3.37$ kbar and higher [Fig. 1(i-j)], ε_1 becomes negative and large for nearly all frequencies indicating purely metallic behavior.

After explaining the experiments, we analyse our observations on the insulating phase in detail, followed by the transition region that exhibits a colossal permittivity enhancement. In a next step, we present our theoretical modelling of the percolative Mott IMT, using a hybrid DMFT approach. Finally our findings and new insight on the Mott transition are discussed comprehensively.

II. EXPERIMENTAL DETAILS

High quality single crystals of κ -(BEDT-TTF) $_2$ -Cu $_2$ (CN) $_3$ were grown by the standard electrochemical synthesis method^{37,38} at the Universität Stuttgart (sample 1) and Argonne National Laboratory (sample 2). In this study we measured the complex electrical impedance as a function of pressure, temperature and frequency in order to obtain the permittivity $\hat{\varepsilon} = \varepsilon_1 + i\varepsilon_2$ or complex conductivity $\hat{\sigma} = \sigma_1 + i\sigma_2$. To that end the crystals are contacted by attaching thin gold wires with carbon paint to opposite crystal surfaces, such that the measurements were performed out-of-plane with $E \perp bc$. The experiments were performed with two contacts in a pseudo four-point configuration³⁹ using an Agilent 4294 impedance analyzer. The applied ac voltage was set to 0.5 V, making sure that we operate in the Ohmic regime. In order to characterize the crystals, we have measured the low-frequency resistivity as a function of temperature and pressure. The results are presented and discussed in detail in Appendix A.

For pressure-dependent dielectric experiments we utilized a piston-type pressure cell ranging up to approximately 10 kbar with a self-made electrical feedthrough for coaxial cables, which is described in detail in Ref. 40. Daphne oil 7373 was used as liquid pressure-transmitting medium because it is inert to molecular solids, has a good hydrostaticity, and stays fluid at room temperature for all applied pressures. The inherent pressure loss upon cooling was recorded *in-situ* by an InSb semiconductor pressure gauge that shows a negligible pressure gradient below $T = 50$ K. As a consequence, in the temperature range of particular interest here, the data are collected in the same pressure cycles; this is important for comparison. Unless indicated otherwise, throughout the manuscript we state the pressure reading at the lowest temperature $T = 10$ K.

The pressure cell was cooled down in a custom-made continuous-flow helium cryostat that allows us to reduce the total cable length to 50 cm enabling reliable measurements at frequencies up to 5 MHz. The compact cryostat design results in a rather steep thermal gradient limiting the lowest reachable temperature to about 8 K. No dependence on the cooling rate was observed, which was kept below 0.4 K/min for all measurements. Since good agreement between the results of both samples was obtained, we present here the data of sample 2. The results obtained on sample 1 are shown in Appendix B.

III. RESULTS AND ANALYSIS

A. Dielectric response in the Mott insulating phase

At reduced temperatures the ambient-pressure dielectric constant $\varepsilon_1(T)$ of κ -(BEDT-TTF)₂Cu₂(CN)₃ reveals a peak, as first reported by Abdel-Jawad *et al.*²⁵ and later confirmed by Pinterić and collaborators²⁶; here, we label this feature as high temperature (HT) peak. When probing with a frequency of $f = 100$ kHz, for instance, the maximum appears at $T = 28$ K, in other crystals up to 40 K, in agreement with previous reports. The observed sample dependence²⁶ is confirmed by disorder studies, which reveal a shift of the maximum in $\varepsilon_1(T)$ to lower temperatures upon x-ray irradiation⁴¹. Fig. 1(a) illustrates how the maximum moves to low temperatures when probed at smaller frequencies; at the same time, however, it gets more pronounced. This behavior resembles the well-known phenomenology of relaxor ferroelectrics⁴².

A closer look reveals a shoulder-like feature around $T = 15$ K, which we denote as low-temperature (LT) mode; it evolves into a small second peak for frequencies between $f = 53$ and 200 kHz. As pressure rises, this LT mode becomes a well-defined peak, it grows in amplitude and eventually dominates the spectrum at $p = 0.86$ kbar, as seen in Fig. 1(c). Although the HT feature seems to maintain its amplitude and width, it becomes secondary. Both modes shift to lower temperatures with pressure (cf. Fig. 5).

For a better understanding of the physical background, we analyse the frequency-dependence of the dielectric response, plotted in Fig. 2 for the example of $T = 14$ K and $p = 0$ kbar. We should note that even at these low temperatures the resistivity of κ -(BEDT-TTF)₂Cu₂(CN)₃ reaches moderate values (cf. Fig. 15); implying that

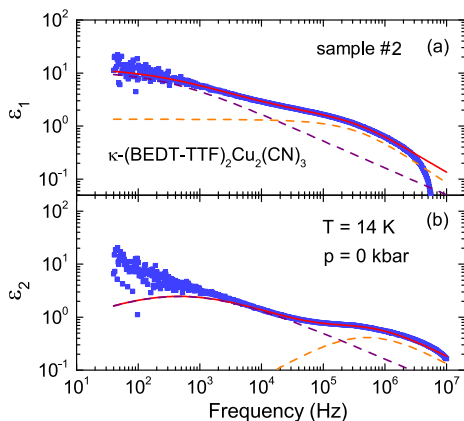


FIG. 2. The real and imaginary part of the dielectric constant of κ -(BEDT-TTF)₂Cu₂(CN)₃, $\varepsilon_1(f)$ and $\varepsilon_2(f)$, as a function of frequency for $T = 14$ K at ambient pressure. The dashed lines represent two Cole-Cole modes; the full lines correspond to their sum according to Eq. (1).

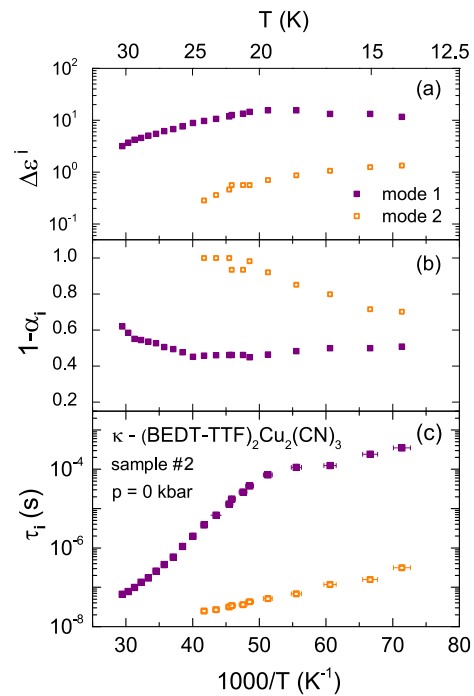


FIG. 3. Arrhenius plots of (a) the dielectric strength $\Delta\varepsilon^{\text{mode } 1}(T)$, (b) the distribution of relaxation times $1 - \alpha(T)$ and (c) the mean relaxation time $\tau(T)$ for both modes obtained from the fits of dielectric data of κ -(BEDT-TTF)₂Cu₂(CN)₃ measured at ambient pressure. The solid purple symbols refer to mode 1 while the open orange squares indicate the data of mode 2.

the dc-conductivity σ_{dc} gives a considerable contribution to the imaginary part of the permittivity. Following the common procedure, we subtract this part: $\varepsilon_2(\omega) = [\sigma_1(\omega) - \sigma_{dc}]/\omega\varepsilon_0$ ^{26,43}. In Fig. 2 we can distinguish two relaxation modes as roll-offs in the real part $\varepsilon_1(f)$ and broad maxima in the imaginary part $\varepsilon_2(f)$. Hence we fit our data by the sum of two Cole-Cole modes:

$$\hat{\varepsilon}(\omega) - \varepsilon_\infty = \frac{\Delta\varepsilon^{\text{mode } 1}}{1 + (i\omega\tau_1)^{1-\alpha_1}} + \frac{\Delta\varepsilon^{\text{mode } 2}}{1 + (i\omega\tau_2)^{1-\alpha_2}}, \quad (1)$$

wherein $\tau_{1,2}$ are the relaxation times, $\omega = 2\pi f$ the angular frequency of the applied electric ac-field, $1 - \alpha_{1,2}$ are real and the parameters describing the symmetric broadening of the relaxation time distribution functions, $\Delta\varepsilon^{\text{mode } 1}$ and $\Delta\varepsilon^{\text{mode } 2}$ are real and denote the dielectric strengths of the corresponding modes, with $\Delta\varepsilon^{\text{mode } 1} + \Delta\varepsilon^{\text{mode } 2} = \varepsilon_{\text{static}} - \varepsilon_\infty$, wherein $\varepsilon_{\text{static}}$ and ε_∞ are the real values for low and high frequencies, respectively. Ambient-pressure studies²⁶ previously identified only a single mode; similar to the related compounds κ -(BEDT-TTF)₂Ag₂(CN)₃³⁵.

In Fig. 3 the parameters obtained from fitting the ambient-pressure data are plotted as a function of inverse temperature. The strength of the first mode $\Delta\varepsilon^{\text{mode } 1}(T)$ shows a peak around $T = 22$ K, resembling $\varepsilon_1(T)$ for low frequencies. The second contribution $\Delta\varepsilon^{\text{mode } 2}$ is approximately one order of magnitude smaller, but increases

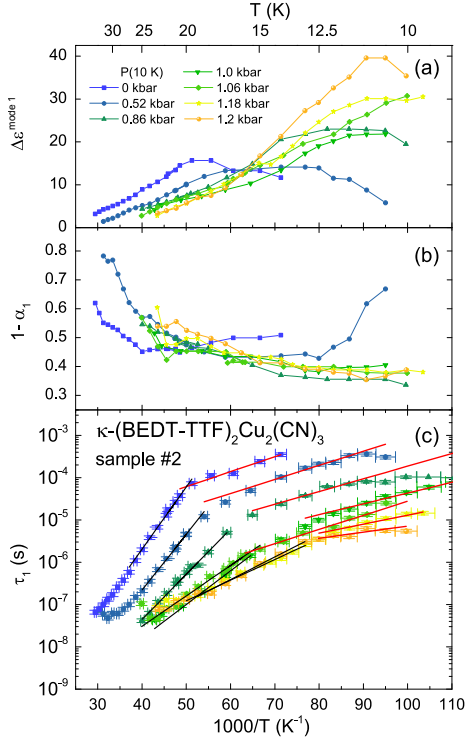


FIG. 4. Arrhenius plots of the Debye parameters of the low-frequency mode 1 in κ -(BEDT-TTF) $_2$ Cu $_2$ (CN) $_3$ for pressures up to 1.22 kbar. (a) Dielectric strength $\Delta\epsilon^{\text{mode } 1}(T)$, (b) distribution of relaxation times $1 - \alpha_1(T)$ and (c) mean relaxation time $\tau_1(T)$. The black and red lines represent fits with Eq. (3) above and below the kink in $\tau_1(T)$ at T_B , respectively.

monotonously upon cooling. With reducing the temperature, $1 - \alpha_1(T)$ decreases and the relaxation time $\tau_1(T)$ increases, providing evidence for significant broadening and slowing down of the dielectric relaxation; in relaxor ferroelectrics this is usually ascribed to cooperative motion and glassy freezing⁴². Interestingly, we observe a kink in τ_1 and a concomitant slight increase of $1 - \alpha_1$ around $T = 20$ K. For the second mode, τ_2 becomes continuously larger as the temperature is reduced, and $1 - \alpha_2$ decreases; again indicating that the corresponding relaxation freezes out.

1. Analysis of Low-Frequency Mode 1

When turning to the pressure dependence, Fig. 4 displays the fit parameters corresponding to mode 1 in an Arrhenius fashion; the presentation is limited to the insulating state with $p \leq 1.2$ kbar. The peak in dielectric strength $\Delta\epsilon^{\text{mode } 1}(T)$ shifts to lower temperatures and increases in amplitude as pressure is applied. This corresponds to the evolution of $\epsilon_1(T)$ plotted in Fig. 1, where the appearance of the LT feature broadens the relaxation. The resulting lower values of $1 - \alpha_1$ do not indicate more cooperativity or glassy behavior compared to ambient pressure. The kink in $\tau_1(T)$ broadens with pres-

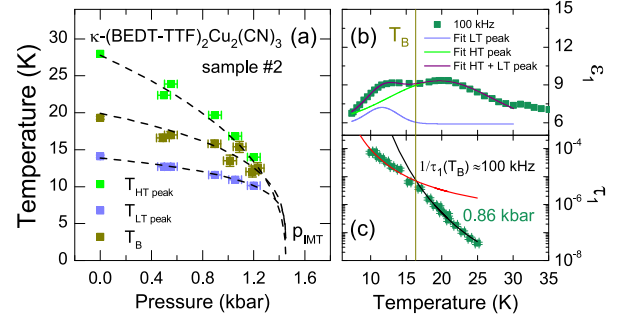


FIG. 5. (a) Pressure dependence of the bifurcation temperature T_B and the positions of the high and low-temperature peak, T_{HT} and T_{LT} , in κ -(BEDT-TTF) $_2$ Cu $_2$ (CN) $_3$; here $p_{\text{IMT}}=1.45$ kbar denotes the critical pressure of the insulator-to-metal transition^{8,37}. (b) For the example of $p = 0.86$ kbar and $f = 100$ kHz the temperature dependence of the dielectric constant $\epsilon_1(T)$ is plotted together with the fits of the HT and LT peak by two Gaussian functions (blue and green lines). (c) The relaxation time $\tau_1(T)$ with the fits from Fig. 4(c) according to Eq. (3) for the temperature range above (black line) and below (red line) the kink at T_B . The crossover from the HT to the LT peak is located at T_B .

TABLE I. Parameters of κ -(BEDT-TTF) $_2$ Cu $_2$ (CN) $_3$ obtained from fits of the pressure evolution of the high-temperature peak T_{HT} , the bifurcation temperatures T_B and the low-temperature peak T_{LT} according to Eq. (2) with $p_{\text{IMT}}=1.45$ kbar. The prefactor A is given in units of $\text{K}\cdot\text{kbar}^{-z}$, while z is a unitless exponent.

	T_{LT}	T_B	T_{HT}
A ($\text{K} \cdot \text{kbar}^{-z}$)	13.0 ± 0.1	18.1 ± 0.2	23.8 ± 0.5
z	0.18 ± 0.01	0.26 ± 0.02	0.41 ± 0.08

sure and shifts to lower temperatures, the corresponding relaxation time gets shorter. A similar feature was previously observed at ambient pressure around $T = 17$ K and attributed to a bifurcation temperature T_B ²⁶; here free charge carriers start to freeze out and hopping-like conduction sets in.

In Fig. 5(b,c), $\epsilon_1(T)$ and $\tau_1(T)$ for $f = 100$ kHz are plotted as a function of temperature at $p = 0.86$ kbar. The HT and LT features in $\epsilon_1(T)$ are well described by two Gaussian functions. Now it becomes clear that the kink in $\tau_1(T)$ at T_B corresponds to the transition from the HT peak to the LT peak with a concomitant change in the relaxation mechanism. We apply this procedure to all pressures and plot the pressure evolution of T_B in panel (a) together with the positions of the peaks at $f = 100$ kHz. The dashed lines represent extrapolations to $p_{\text{IMT}} = 1.45$ kbar^{8,37} according to

$$T_i = A \cdot (p_{\text{IMT}} - p)^z, \quad (2)$$

with $i = \{\text{HT}, \text{B}, \text{LT}\}$ the three characteristic temperatures, A being a coefficient in units of $\text{K}\cdot\text{kbar}^{-z}$ and z the critical exponent. The obtained parameters are listed in Table I.

For $T > T_B$, we can describe the dependence of the relaxation time τ_1 on temperature by an activated behavior

$$\tau_1 = \tau_{HT} \exp\{\Delta_{HT}/T\} \quad , \quad (3)$$

which is represented by the black lines in Fig. 4(c). The low-temperature regime can be also fitted with an activated behavior in analogy to Eq. (3), which is illustrated by the red lines in Fig. 4(c).

The extracted fit parameters for the HT mode ($T > T_B$) and the LT mode ($T < T_B$) are plotted in Fig. 6 as a function of pressure; here we also include the qualitatively similar results obtained from sample 1 while the corresponding plots are presented in the Appendix B. Our findings are in line with previous ambient-pressure studies²⁶. $\Delta_{HT}(p)$ decreases as pressure rises following a mean-field behavior in analogy to Eq. 2. Best fits were obtained by using fixed $p_{IMT,2} = 1.45$ kbar and $p_{IMT,1} = 1.05$ kbar for sample 2 and sample 1, respectively, as obtained from their phase diagrams, which are discussed in detail in Appendix A. The fit parameters are summarized in Table II and show good agreement between the two samples for the critical exponents.

$\Delta_{LT}(p)$ [Fig. 6(c)] is constant up to $p = 1.1$ kbar, followed by a strong decrease when the pressure is further increased. The behavior is reminiscent of a first-

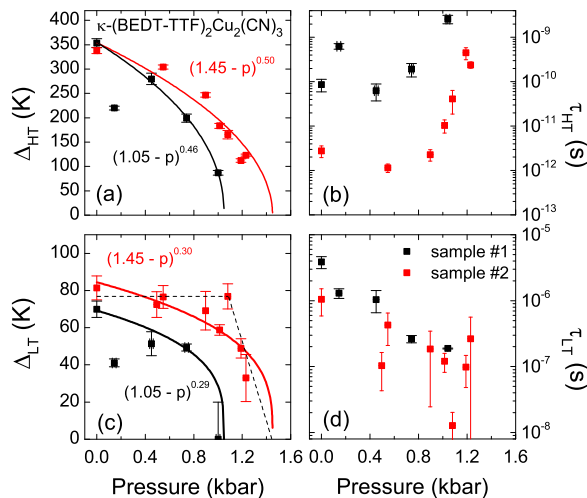


FIG. 6. Pressure dependence of the activation energy and relaxation time of κ -(BEDT-TTF) $_2$ Cu $_2$ (CN) $_3$ obtained from fits of the corresponding temperature behavior of $\tau_1(T)$ shown in Fig. 4(c). The upper panels (a,b) correspond to the high-temperature regime; the lower panels (c,d) to the low-temperature regime. (a) The activation energy Δ_{HT} and (b) the time scale τ_{HT} for the ac response in the high-temperature limit; (c) the pressure evolution of Δ_{LT} and (d) of τ_{LT} , respectively. The black symbols correspond to sample 1, the red symbols to sample 2 while the solid lines represent mean-field fits in analogy to Eq. 2. Most importantly, Δ_{LT} seems to be constant and abruptly decreases around 1.1 kbar, reminiscent of a first-order phase transition with $p_{IMT} = 1.45$ kbar.

TABLE II. Mean field parameters A and z of Δ_{HT} and Δ_{LT} in analogy to Eq. (2) using fixed $p_{IMT,2}=1.45$ kbar and $p_{IMT,1} = 1.05$ kbar for sample 2 and sample 1, respectively.

sample 2	Δ_{HT}	Δ_{LT}
A (K · kbar $^{-z}$)	294 ± 16	75 ± 2
z	0.50 ± 0.09	0.30 ± 0.04
sample 1	Δ_{HT}	Δ_{LT}
A (K · kbar $^{-z}$)	347 ± 5	68 ± 4
z	0.46 ± 0.03	0.29 ± 0.05

order phase transition and extrapolates to $\Delta_{LT} = 0$ at $p_{IMT} = 1.45$ kbar; in excellent agreement with the findings in Fig. 5. For sample 1, it is difficult to pin down whether Δ_{LT} follows mean-field behavior or not because the number of data points is limited. Since Δ_{HT} and T_B both follow mean-field behavior, we also apply a tests for mean-field behavior on Δ_{LT} , represented by the solid lines, which seems less reasonable for sample 2.

The time scale τ_{HT} [Fig. 6(b)] becomes longer upon applying pressure; there seems to be a rather strong sample dependence. The characteristic time τ_{LT} [Fig. 6(d)] seems to decrease upon applying pressure. Both samples agree well in the overall behavior and absolute values.

2. Analysis of High-Frequency Mode 2

In the Arrhenius plot of Fig. 7 we show the parameters of the second mode $\Delta\varepsilon_2(T)$, $1 - \alpha_2(T)$ and $\tau_2(T)$ as obtained from the Cole-Cole fits. Throughout the whole pressure-temperature range wherein mode 2 is observed, its strength $\Delta\varepsilon^{\text{mode } 2}$ stays an order of magnitude below the one of the low-frequency mode 1. $\Delta\varepsilon^{\text{mode } 2}(T)$ increases steadily as the temperature is reduced. With rising pressure the mode shifts to lower temperatures (Fig. 1) and correspondingly does the enhancement in $\Delta\varepsilon^{\text{mode } 2}(T)$. A drop in $1 - \alpha_2(T)$ indicates a considerable broadening of the mode. The temperature dependence of τ_2 is strongly influenced by pressure. While at ambient pressure $\tau_2(T)$ monotonically increases, at $p = 0.52$ kbar a minimum is observed that shifts to lower temperatures and gets more pronounced at $p = 0.86$ kbar. In other words, $\tau_2(T)$ depends on pressure in a non-monotonic way. A similar relaxation dynamics has been widely observed for confined systems as well as in the relaxor ferroelectric KTa $_{0.65}$ Nb $_{0.35}$ O $_3$ when doped with Cu by approximately 0.1%⁴⁴.

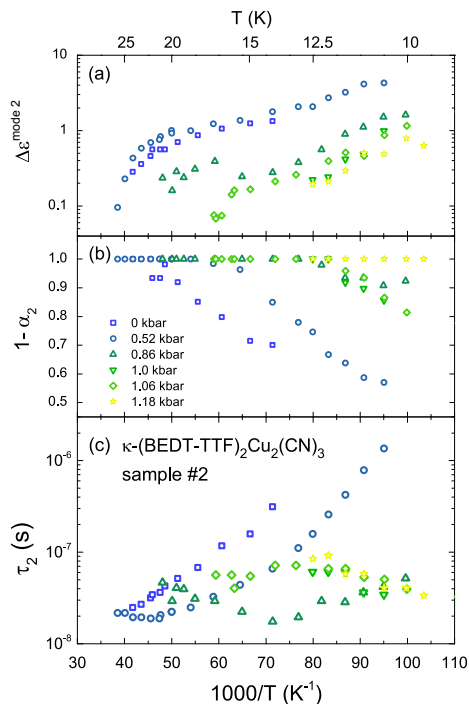


FIG. 7. Temperature dependence of the parameters describing mode 2 in κ -(BEDT-TTF)₂Cu₂(CN)₃ at various pressures. (a) Dielectric strength $\Delta \epsilon^{\text{mode } 2}$, (b) distribution of relaxation times $1 - \alpha_2$ and (c) mean relaxation time τ_2 in an Arrhenius plot versus inverse temperature. Upon increasing pressure, a pronounced minimum in τ_2 develops, indicating a non-monotonic relaxation dynamics in κ -(BEDT-TTF)₂Cu₂(CN)₃.

B. Dielectric response at the insulator-metal transition

1. Percolation transition and effective medium approach

The most surprising observation of Fig. 1 is the dramatic increase of the dielectric constant of κ -(BEDT-TTF)₂Cu₂(CN)₃ for $p > 1.2$ kbar. To articulate the behavior more clearly, in Fig. 8 we plot the pressure dependence of $\epsilon_1(p)$ and $\sigma_1(p)$ as obtained for a fixed frequency $f = 100$ kHz at different temperatures. A pronounced peak in the permittivity appears around 1.8 kbar followed by a drop to negative values evidencing the onset of metallic conduction. We explain this observation by percolation when the insulator-metal phase boundary is approached: metallic puddles develop within the insulating matrix and grow with increasing pressure.

At the lowest temperature, $T = 10$ K, the peak maximum occurs at a pressure slightly above p_{IMT} . This can be understood when recalling the definition of the percolation threshold as the first continuous conducting path, while the dielectric constant is integrated over the entire volume; hence the overall capacitance still increases even when some inclusions already coalesce. As seen from Fig. 8(a), the peak in $\epsilon_1(p)$ shifts to even higher

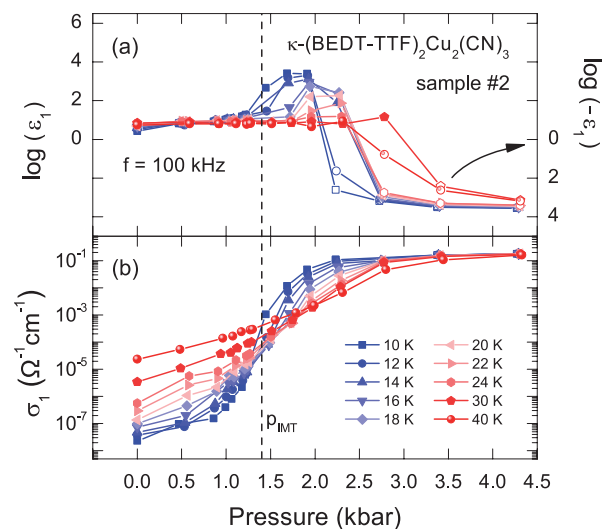


FIG. 8. Pressure dependence of the dielectric properties of κ -(BEDT-TTF)₂Cu₂(CN)₃ recorded for a fixed frequency $f = 100$ kHz at different temperatures. (a) The permittivity ϵ_1 forms a pronounced maximum followed by a rapid drop to negative values. (b) The conductivity σ_1 exhibits a step-like increase with an inflection point located right at the onset of the peak in ϵ_1 . This percolating behavior stems from the nucleation and growth of metallic puddles spatially separated in an insulating matrix; the filling fraction increases by applying pressure. With rising temperature the features shift to higher pressures and diminish in amplitude and step size, respectively.

pressure values as T rises, but strongly diminishes upon heating; for $T > 22$ K the anomaly is completely suppressed. Eventually a simple drop in permittivity remains with a change in sign to large negative values of $\epsilon_1(p = 43 \text{ kbar}) \approx -10^3$ to -10^4 .

The enhancement of the dielectric constant is accompanied by a step-like feature in the conductivity, presented in Fig. 8(b). With pressure, the metallic fraction grows; consequently $\sigma_1(p)$ rises continuously until a saturation is reached in the metallic phase where the pressure-dependence of the conductivity is minuscule. The inflection point corresponds to p_{IMT} , defined above by dc-resistance measurements⁸. With rising temperature, the step feature shifts to higher pressure values, smears out and becomes a more gradual increase consistent with the change from the first-order IMT to the crossover region upon heating through T_{crit} .

If the pressure-driven IMT in our Mott system is a first-order transition for $T < T_{\text{crit}}$, two phases are thermodynamically stable in the coexistence region^{45,46}: One represents the metallic state while the other corresponds to the insulating phase. In the presence of weak disorder, such a region will feature a mixture of randomly distributed metallic and insulating domains, with respective volume fractions that vary with pressure. The IMT takes place when the volume fraction of the metallic phase approaches the percolation threshold. The dielectric prop-

erties of the mixture are captured by Bruggeman's effective medium approximation (BEMA)^{47–49}:

$$x \frac{\varepsilon_m - \varepsilon_{\text{eff}}}{\varepsilon_{\text{eff}} + L(\varepsilon_m - \varepsilon_{\text{eff}})} + (1 - x) \frac{\varepsilon_i - \varepsilon_{\text{eff}}}{\varepsilon_{\text{eff}} + L(\varepsilon_i - \varepsilon_{\text{eff}})} = 0 \quad , \quad (4)$$

where x is the volume fraction of the metallic inclusions, L is the shape factor, ε_i and ε_m are the complex permittivities of the insulating and metallic phases, respectively, and ε_{eff} is the effective permittivity of the composite.

2. Divergent dielectric constant

The dielectric properties of percolating systems have been subject of numerous investigations for half a century^{48,50}. As pointed out by Efros and Shklovskii⁵¹ the static dielectric constant of a percolating system is a function of the filling fraction x of the metallic phase and diverges at the percolation threshold x_c :

$$\varepsilon_1(\omega \rightarrow 0, T \rightarrow 0, x) \propto (x_c - x)^{-q} \quad , \quad (5)$$

where the critical exponent q depends on the dimension of the system; in three dimensions we expect q ranging from 0.8 to 1^{51–54}, while $q = 1.3$ is calculated for two dimensions⁵¹. The BEMA model predicts $q = 1$ independent of the dimensionality of the percolating system⁵³.

The divergency gets reduced and rounded as the insulating matrix acquires a finite conductivity σ_i , for instance as temperature rises:

$$\varepsilon_1(T, x_c) \propto \left[\frac{\sigma_m(T)}{\sigma_i(T)} \right]^{1-s} \quad , \quad (6)$$

where $s = 0.5$ and 0.62 in two and three dimensions, respectively⁵¹, and σ_m denotes the conductivity of the metallic regions. Although our data do not permit a quantitative comparison, the observed reduction of the peak seen in Fig. 8(a) is in accord with the tendency of Eq. (6).

Even for complete insulators, a reduction of the peak amplitude is expected when probed at finite frequencies, according to⁵¹

$$\varepsilon_1(\omega, x_c) \propto (1/\omega)^{1-s} \quad . \quad (7)$$

Choosing the pressure for which the dielectric constant reaches the maximum value, in Fig. 9 we plot the frequency-dependence of $\varepsilon_1(\omega, p = 1.7 \text{ kbar})$ for several temperatures. For $T \leq 16 \text{ K}$, $\varepsilon_1(\omega)$ strongly drops with frequency following a power-law for two orders of magnitude before it levels off at $\omega/2\pi \approx 2 \text{ MHz}$. In the vicinity of the critical endpoint and above T_{crit} , the percolative behavior vanishes and merges into a frequency-independent response. Following Eq. (7), we fit the data in Fig. 9 and obtain an exponent $1 - s$ for each temperature, displayed in the inset. The deviation from theory has several reasons: standard percolation theory does

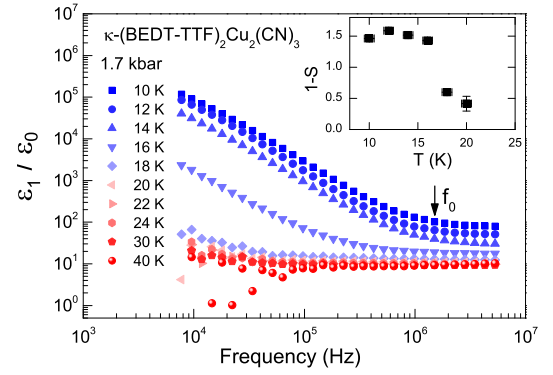


FIG. 9. Double-logarithmic plot of $\varepsilon_1(f)$ at 1.7 kbar for various temperatures, as indicated. For $T \leq 16 \text{ K}$ a power-law behavior is observed, which saturates above $f \approx 2 \text{ MHz}$. The percolating behavior of $\kappa\text{-(BEDT-TTF)}_2\text{Cu}_2(\text{CN})_3$ is suppressed for $T > 16 \text{ K}$ where the first-order transition becomes a gradual crossover. The inset shows the temperature dependence of the exponent $1 - s$ obtained from fits by Eq. (7).

not take into account field enhancement effects between adjacent finite metallic clusters beyond the dipole approximation and/or hopping of charge carriers between them as well as electron-electron interactions, as pointed out previously^{55–58}. Sarychev and Brouers⁵⁹ explicitly account for tunneling between finite metallic clusters in order to explain the low-frequency response of percolating systems.

3. Estimate of the metallic filling fraction from experimental results

In Fig. 10(a) and (b) the real and imaginary parts of the dielectric constant of $\kappa\text{-(BEDT-TTF)}_2\text{Cu}_2(\text{CN})_3$ are plotted as a function of pressure measured at various frequencies at the lowest accessible temperature. With increasing frequency we find the peak in $\varepsilon_1(p)$ diminishing and getting round. At the same time, the step in $\sigma_1(p)$ becomes less pronounced.

If we assume that for $p = 0$ the specimen is completely in the insulating phase, the properties resemble ε_i ; for $p = 4.3 \text{ kbar}$ the metallic state is fully established, corresponding to ε_m . We can now obtain the metallic filling fraction x for each particular pressure value that best describes the experimentally determined complex permittivity by the effective permittivity ε_{eff} calculate via Eq. (4) assuming spherical inclusions: $L = 1/3$. In Fig. 10 the respective fits are shown by solid lines for the various frequencies. At these low temperatures, the effective-medium model yields reasonable fits to the real part of the permittivity ε_1 for the low-pressure data. The resulting filling fraction x is plotted in Fig. 10(c) as a function of pressure. The gradual increase follows a tanh-like behavior around the IMT, supporting our assumption for the theoretical simulations below [Eq. (10)].

As already noted above, the peak in $\varepsilon_1(p)$ occurs at

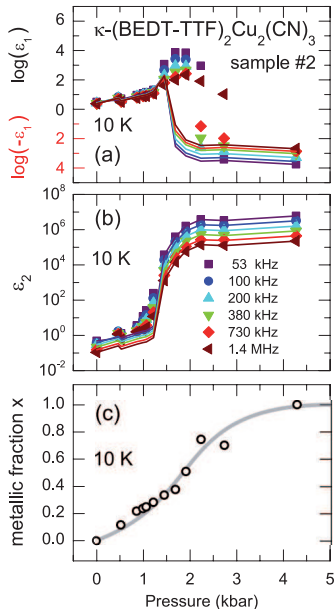


FIG. 10. (a,b) Pressure dependence of the permittivity of κ -(BEDT-TTF)₂Cu₂(CN)₃ measured at $T = 10$ K using different frequencies as indicated. The solid lines represent fits by Bruggeman’s effective medium approximation [Eq. (4)] for spherical inclusion with the fraction of filling fraction as free parameter. (c) The metallic fraction x in dependence of pressure exhibits a rapid change around the percolation; the gray line is a guide to the eye.

slightly higher pressure than the steep increase in $\epsilon_2(p)$, which is not captured by simple percolation theory. In part it results from the integral measurement of our macroscopic specimen, where the overall capacitance still grows despite the increasing conducting areas. These effects are beyond BEMA and might be addressed in future studies. We further expect this method to severely overestimate the extent of the coexistence regime because the pressure dependence of the conduction properties is neglected. A narrower region of around 1 to 2 kbar is more likely. In the following section III C we address this issue by theoretical modeling. We determine the complex permittivity of the mixed phase by calculating first the pure phases, together with their full correlation dependence, and then embedding them in a percolating network.

Now that we obtained the pressure-dependence of the metallic filling fraction $x(p)$, we are in the position to analyse $\epsilon_1(x)$. The corresponding plot for the 100 kHz data is shown in Fig. 11(a) together with the fits according to Eq. (5). The temperature dependence of the percolation threshold x_c and the exponent q is presented in Fig. 11(b) and (c), respectively. Percolation is established at a critical filling fraction $x_c \approx 0.35$, in excellent agreement with the prediction of $\frac{1}{3}$ for a three-dimensional system. From our pressure-dependent dielectric measurements we find $q \approx 1$ up to T_{crit} as expected within the BEMA framework.

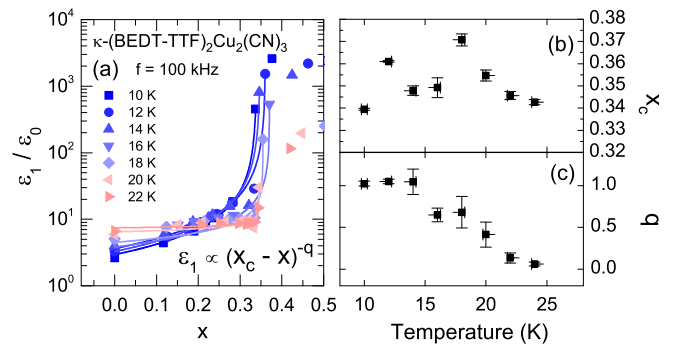


FIG. 11. (a) Dielectric constant ϵ_1 of κ -(BEDT-TTF)₂Cu₂(CN)₃ measured at $f = 100$ kHz for several temperatures in dependence of the relative pressure ($p - p_c$). The solid lines represent fits according to Eq. 5. (b) Temperature dependence of the percolation threshold p_c , as obtained from the fits in (a). (c) Temperature dependence of the exponents q . We attribute the drop of q above T_{crit} to the change from the first-order insulator-metal transition to a crossover at higher temperatures. For clarity reasons, we also include $T_{\text{crit}} = 16$ K (dashed red line) and the predictions for q according to the BEMA model (dashed blue line).

C. Theoretical analysis of the dielectric permittivity at the IMT

We have just established a way to estimate ϵ_{eff} of this percolative first-order insulator-metal transition (IMT) provided we know the properties of the constituting phases. Now we want go this avenue on purely theoretical ground. To that end, we calculate $\epsilon_m(\omega, T)$ and $\epsilon_i(\omega, T)$ of the pure metallic and insulating phases and use them to obtain the electrodynamic properties of the mixture via Eq. (4). We assume a half-filled Hubbard model in two dimensions with semicircular bands and apply dynamical mean-field theory (DMFT) calculations. Within the single site DMFT approach, the real part of optical conductivity $\sigma_1(\omega)$ is given by the expression^{45,60,61}

$$\begin{aligned} \sigma_1(\omega) &= \frac{2e^2}{\pi\hbar} \frac{1}{a} \frac{1}{S} \int dE \rho_0(E) [V(E)]^2 \\ &\times \int_{-\infty}^{+\infty} d(\hbar\nu) \frac{f(\hbar\nu) - f(\hbar\nu + \hbar\omega)}{\hbar\omega} \\ &\times \text{Im} \{G(\hbar\nu + \hbar\omega, E)\} \text{Im} \{G(\hbar\nu, E)\}, \end{aligned} \quad (8)$$

where

$$G(\hbar\nu, E) = \frac{1}{\hbar\nu - E - \Sigma(\hbar\nu)},$$

is the Green function and $\Sigma(\hbar\nu)$ is the local self energy. The imaginary part of the optical conductivity $\sigma_2(\omega)$ is then calculated via Kramers-Kronig transform⁶⁰:

$$\sigma_2(\omega) = -\frac{2}{\pi} \int_0^\infty \frac{\omega' \sigma_1(\omega')}{\omega'^2 - \omega^2} d\omega' \quad . \quad (9)$$

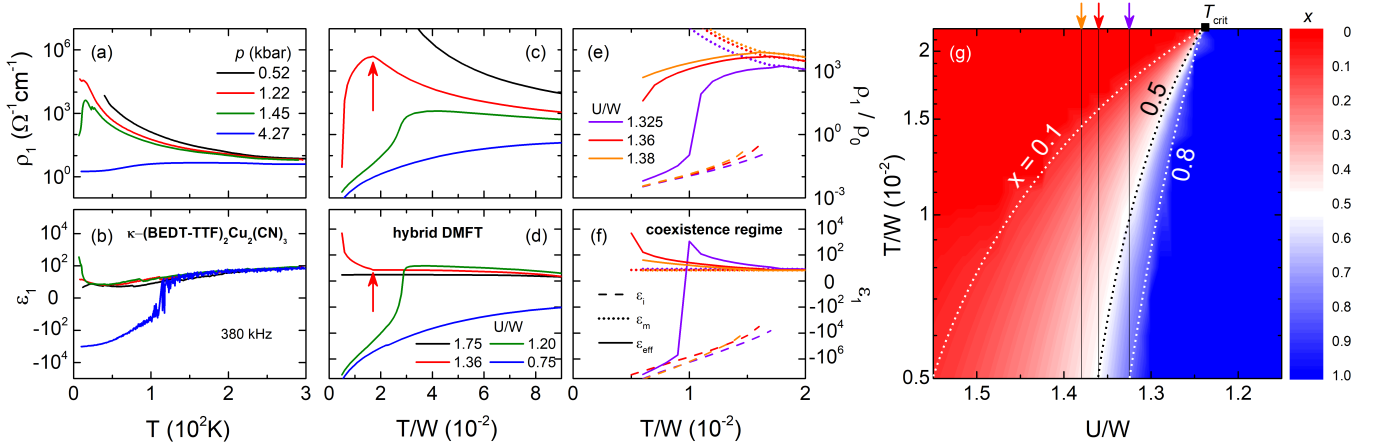


FIG. 12. (a,b) Pressure evolution of the temperature dependent resistivity and permittivity measured at $f = 380$ kHz along the a -axis of κ -(BEDT-TTF) $_2$ Cu $_2$ (CN) $_3$. (c,d) Calculated resistivity and permittivity using hybrid DMFT with different strength of effective correlations U/W as indicated. The red arrows indicate the temperature below which the coexistence regime is entered. (e,f) For selected values of U/W close to the Mott insulator-to-metal transition the temperature dependent resistivity and permittivity is plotted for the insulating phase, ε_i (dotted lines), the metallic phase ε_m (dashed lines) and the resulting effective medium ε_{eff} (solid lines) at lowest temperatures in the coexistence regime. (g) Volume fraction x of the metallic component in a false-color presentation according to the right scale. The dependence on correlation strength U and temperature T , normalized to the bandwidth W , is calculated by Eq. (10). The dotted lines represent $x = 0.1, 0.5$ and 0.8 . Since in our model $L = \frac{1}{2}$, the metallic domains stop connecting at $x = 0.5$; here the conductivity drops sharply. The black solid lines indicate the effective correlation strength used for calculating the temperature dependence of $\rho_1(T)$ and $\varepsilon_1(T)$ shown in panels (e) and (f) by purple, red and orange colors.

Applying these expressions (8) and (9), we obtain the complex dielectric response $\hat{\varepsilon}(\omega) = 1 + i\hat{\sigma}(\omega)/\omega\varepsilon_0$, via DMFT across the entire phase diagram, as a function of temperature T and the interaction U . We stress that within the coexistence region we find two locally stable solutions, while outside there is only one solution. In Eq. (8), $a = 15\text{\AA}$, is the distance between layers for our material³⁷, yielding a sheet conductance $e^2/(ha) \approx 260 (\Omega\text{cm})^{-1}$. $V(E)/\sqrt{S}$ is the current vertex, which is equal to $\sqrt{(D^2 - E^2)/3}$, and $\rho_0(E) = 2\sqrt{D^2 - E^2}/\pi D^2$ is the semicircular model density of states of non-interacting electrons of bandwidth $W = 2D$.

In order to calculate the total dielectric function within the (percolating) coexistence region, we not only have to know the dielectric function for each of the two phases, ε_i and ε_m , but also the relative volume fraction of the two components as a function of temperature T and effective correlations U/W . For simplicity, we use a hyperbolic tangent function to represent the metallic volume fraction x :

$$x\left(\frac{T}{W}, \frac{U}{W}\right) = \frac{1}{2} \tanh\left\{\frac{c[(U/W)_{\text{crit}} - (U/W)]}{(T/W)_{\text{crit}} - T/W}\right\} + \frac{1}{2}, \quad (10)$$

which is centered around $(U/W)_{\text{crit}} = (0.20 - T/W)/0.14$, as depicted in Fig. 12(g). The behavior is in accord with our analysis of the experimental findings, shown in Fig. 10(c). We also select $c = 0.1$ for $U/W > (U/W)_{\text{crit}}$ and $c = 0.3$ for $U/W < (U/W)_{\text{crit}}$ as

expected from the DMFT phase diagram^{10,46}.

Finally, we obtain the optical conductivity $\sigma_1(\omega, T)$ and dielectric permittivity $\varepsilon_1(\omega, T)$ inside the coexistence region via the BEMA Eq. (4). We assumed $L = \frac{1}{2}$ for our calculations, but the findings can be easily scaled to $L = \frac{1}{3}$. Here we focus on very low frequency $\omega/2\pi = 10^{-9}W \approx 320$ kHz, in order to allow comparison of the calculated permittivity with our experiments. For better relating our calculated to experimental results, in Fig. 12 we plot representative curves of electrical resistivity $\rho_1(T)$ and dielectric permittivity $\varepsilon_1(T)$ for various correlation strengths U covering the insulating, percolating and metallic regions of the phase diagram. For large U/W the system behaves insulating with a small positive dielectric constant, corresponding to the behavior observed at ambient and low pressure ($p < 1$ kbar). For intermediate correlation strength $U/W = 1.36$, the resistivity starts insulating at high temperatures, but $\rho_1(T)$ exhibits a maximum around $T/W \approx 1.6$ below which it turns weakly metallic. Upon cooling the system enters the coexistence regime with metallic inclusions, as depicted in Fig. 12(g). Around that temperature, $\varepsilon_1(T)$ rises rapidly, acquiring 10^4 near the percolation threshold. This temperature dependence resembles the observations on κ -(BEDT-TTF) $_2$ Cu $_2$ (CN) $_3$ for $p = 1.45$ kbar. As U/W decreases further, the phase boundary to the metallic phase is crossed with a drop in $\rho_1(T)$ and a sign change in the dielectric constant. For $U/W = 1.75$ metallic properties are found in the entire temperature range. This behavior is reached for the highest pressure values

above 4 kbar. The full set of data is presented in Figs. 15 and 1.

Here we want to focus on the regime right at the IMT and therefore plot the behavior for U/W close to the critical correlation strength. In Fig. 12(e) and (f) the properties $\rho_1(T)$ and $\varepsilon_1(T)$ of the constituting insulating and metallic phases are plotted together with the effective behavior ε_{eff} . The coexistence regime is entered around $T/W = 0.016$ to 0.018 – the particular value depends on the effective correlations U/W according to Eq. (10) – and there the resistivity drops, accompanied by a change in sign of the dielectric constant to large negative values due to screening in the metal. For $U/W = 1.325$ the metallic state is reached only at significantly lower temperatures, corresponding to the slope of the phase boundary in depicted in Fig. 12(g).

IV. DISCUSSION

A. Dielectric relaxation in the insulating state

1. High-temperature peak

Our pressure-dependent investigations unveil that the dielectric response of κ -(BEDT-TTF)₂Cu₂(CN)₃ contains two dielectric contributions. The high-temperature (HT) peak was first observed by Abdel-Jawad *et al.*²⁵, but there is no consensus on its origin. The dimer approach takes the BEDT-TTF dimer as an entity, neglecting the intra-dimer degrees of freedom; this leads to a quasi two-dimensional electron system with a half-filled conduction band, where on-site Coulomb repulsion dominates making κ -(BEDT-TTF)₂Cu₂(CN)₃ to a prime example to study the genuine Mott physics⁹. Alternatively, one considers a single BEDT-TTF molecule with certain inter- and intra-dimer interactions. As a consequence, κ -(BEDT-TTF)₂Cu₂(CN)₃ is regarded as a $\frac{3}{4}$ -filled system, making it unstable towards a charge-ordered state, which is competing with the dimer Mott insulating state. Starting from the quarter-filled extended Hubbard model, theory predicts fluctuating charge disproportionation within a dimer giving rise to quantum electric dipoles^{27,28}. The dielectric response in the audio- and radio-frequency range was interpreted as a consequence of these electric dipoles^{25,27–30}; their collective optical excitations should show up in the THz region.

However, infrared and vibrational spectroscopy clearly discards a sizable charge disproportionation on the dimers³²; a mixture of lattice and molecular vibrations perfectly explains all the observed modes even below 1 THz¹⁶. In a recent theoretical study⁶² Fukuyama *et al.* considered the crossover from a quarter-filled system with charge-ordered ground state to the dimer Mott insulator due to strong dimerization. At high energy (in the range of eV, i.e. optical frequencies) the dimer Mott insulator is stable, whereas at very low energy (10^{-10} eV \approx 10 kHz) charge order becomes dominant leading to extended do-

main of different charge polarities. As a consequence, domain walls form in the system, giving rise to the HT peak. Very recently, Pouget and collaborators¹⁸ thoroughly investigated the crystal structure of κ -(BEDT-TTF)₂Cu₂(CN)₃ and discovered a triclinic symmetry with two inequivalent dimers in the unit cell. This implies a rather weak charge imbalance between dimers in the whole temperature range.

During the last years evidence has accumulated that the interaction between the cationic (BEDT-TTF)₂⁺ and the anionic Cu₂(CN)₃⁻ layer is crucial for the understanding of these charge-transfer salts^{16,18,26}. The ambiguity in the arrangement of the polar CN⁻ linking the triangular coordination of Cu atoms results in intrinsic disorder. Density functional theory calculations estimate that flipping a CN link, which is mainly oriented along the b -direction costs 174 meV, whereas flipping one that is mainly oriented along the c -direction is only 10-15 meV¹⁶. The interaction via hydrogen bonds maps the domains onto the BEDT-TTF layer, leading to long-range charge inhomogeneities that are subject to low-frequency probes in the kHz and MHz range²⁶.

The extension of the relaxation time τ_{HT} and decrease of Δ_{HT} as pressure rises indicate that the domains increase in size and are easier to move. On the other hand, a decrease of τ_{HT} and barrier energy E_{VFT} upon x-ray irradiation, reported by Sasaki *et al.*⁴¹, infer more domains of smaller size. This can be explained by a larger number of charged defects in the anion layer upon irradiation which act as pinning centers. The qualitatively similar but quantitatively slightly different behavior found in our sample 1 (Fig. 17) corroborates these observations.

It is interesting to recall that also x-ray irradiation leads to a shift of the HT peak to lower temperatures⁴¹. High-energy irradiation causes crystal defects mainly in the anion layer and is supposed to increase the number of charge carriers. Similar to the rising pressure, the conductivity of the sample is enhanced compared to the pristine case. This clearly indicates that the relaxor-ferroelectric HT peak is influenced by screening due to free charge carriers, disentangling it from an intrinsic origin related the conduction electrons themselves, thus rendering a scenario of intra-dimer dipoles unlikely.

2. Low-temperature peak

Let us come to the LT peak, which was not observed in previous ambient pressure studies of κ -(BEDT-TTF)₂-Cu₂(CN)₃^{25,26,41}. Consistently, in both samples under inspection, we see a remarkable growth of the LT peak with pressure and a shift in its position as shown in Fig. 5. The clearly distinct pressure evolution of the LT parameter compared to the HT peak (Fig. 6) indicates a different origin. As can be seen from Fig. 5, the peak appears only below the critical temperature T_{crit} , i.e. in the range of spatially coexisting metallic inclusions in an insulating host, even below the complete percola-

tion. For $T < T_{\text{crit}}$, the pressure evolution of $\varepsilon_1(p)$ upon approaching the phase boundary includes the LT-peak can be well fitted by Eq. (5), as expected for a percolating system (Fig. 11). Hence we can confirm previous suggestion of metallic quantum fluctuations drawn from optical spectroscopic studies at ambient pressure⁹. The low-temperature peak grows towards the phase transition and eventually becomes the dominant peak at the percolation threshold, as seen in Fig. 1.

The energy Δ_{LT} stays constant up to the IMT, where $\varepsilon_1(p)$ is reproduced very well by the BEMA model (Fig. 10) – the latter does not consider a capacitive coupling of the metallic inclusions. Hence, we attribute the drop in Δ_{LT} close to the percolation threshold to an increased coupling between the metallic inclusions. With values of τ_{LT} decreasing from 10^{-6} to 10^{-8} s, the LT relaxation is clearly slower than the HT peak; it hardens upon increasing x . The origin of this intriguing behavior has yet to be clarified, i.e. whether this can be assigned to changes in size and/or shape of the metallic inclusions. Such a behavior was revealed by ellipsometric studies of VO_2 films⁶³.

At this point it is worthwhile to mention that the LT peak is reminiscent of the dielectric response in the related compound $\kappa\text{-(BEDT-TTF)}_2\text{Cu}[\text{N}(\text{CN})_2]\text{Cl}$ ^{34,64,65}, which is very close to the metal insulator transition already at 0 kbar. This enables investigations of the LT peak and the nature of the metallic inclusions at ambient pressure via a broad spectrum of experimental techniques, such as scanning near-field infrared microscopy⁶⁶. Deuterating $\kappa\text{-(BEDT-TTF)}_2\text{Cu}[\text{N}(\text{CN})_2]\text{Br}$ crystals is another way to approach the metal-insulator transitions. In these systems Sasaki *et al.* succeeded to spatially map micrometer size domains using infrared spectroscopy⁶⁷. However, the insulating ground state is an antiferromagnet, and hence the phase boundary has opposite slope due to the Clausius-Clapeyron relation.

B. Dielectric catastrophe

The transition from insulating to metallic conduction properties occurs in condensed-matter physics in numerous forms⁶⁸. Doping silicon with phosphorous, for instance, turns it metallic as the amount of electron donors exceeds a critical concentration $N_c = 3.5 \times 10^{18} \text{ cm}^{-3}$ ^{50,69}. The transition between localized and metallic phases in disordered electronic systems is known as Anderson transitions^{70,71}. Random systems or networks form long-range connectivity when crossing the percolation threshold; extended scaling theories have been developed but the details strongly depend on the particular lattice and dimension^{48,72,73}. The formation of density waves due to Fermi surface nesting – in particular in low-dimensional solids – leads to the opening of a gap in the density of states^{74,75}. In the present case of a Mott transition, electron-electron interaction causes the metal to become insulating. The transition can be

driven by either varying the electron density N or the interaction strength U ^{76–78}.

Besides the usual thermodynamic signatures of phase transitions, the experimental hallmark of all of these insulator-to-metal transitions is the drop in resistivity, often by many orders of magnitude upon changing the order parameter or temperature. In addition, a divergence of the static dielectric constant is predicted by classical percolation theory when approaching the transition from either side, with some characteristic scaling behavior^{51,53,79–81}. Experimentally Castner *et al.* first observed a strong increase of the static dielectric constant at a critical concentration N_c when they measured n -doped silicon in the kHz range at low temperatures⁸²; systematic studies of P:Si^{83,84} revealed $\varepsilon_1 - \varepsilon_{\text{host}} \propto (N_c/N - 1)^{1.2}$. Most investigations deal with composite materials, such as microemulsions^{85–88}, composites^{89,90} or percolating metal films^{54,91,92}.

In many cases the metal-insulator transition is only crossed by lowering the temperature; here thermal fluctuations and inhomogeneities may occur. The situation is distinct from investigations of the phase coexistence by tuning the effective correlation strength via pressure in the limiting case of $T \rightarrow 0$. Tanner and collaborators⁹³, for instance, analyzed their temperature-dependent measurements on the charge-density wave transition in TTF-TCNQ using a self-consistent effective medium approximation⁴⁷. Temperature-dependent near-field infrared microscopy of Qazilbash *et al.*^{66,94} on VO_2 films actually maps the spatial phase separation, and they extract a divergence of the dielectric constant at the transition temperature. In the case of the high-temperature Mott transition of V_2O_3 , Limelette *et al.* concluded the coexistence region close to the critical endpoint at 458 K from the hysteresis in the pressure-dependent conductivity curves⁹⁵. From transport measurements on $\kappa\text{-(BEDT-TTF)}_2\text{Cu}_2[\text{N}(\text{CN})_2]\text{Cl}$ similar conclusions were drawn on the coexistence of Mott insulator and correlated metal⁶. In addition, NMR experiments revealed the coexistence of antiferromagnetism and superconductivity, as well as a hysteresis in susceptibility⁵.

Considering the IMT in doped semiconductors, Sir Nevill Mott termed the divergence of the electric susceptibility ‘dielectric catastrophe’ only in the second edition of his seminal monograph on the metal-insulator transition⁶⁸. Beyond percolation and polarization issues, he pointed out the importance of the localization length ξ and electronic interaction. Aebischer *et al.* came back to this idea and theoretically analyzed the $\varepsilon_1 \propto \xi^2$ behavior when approaching the Mott transition from the insulating side⁹⁶. These situations are distinct from the present case, where phase coexistence causes the permittivity enhancement at the first-order IMT.

Record-high dielectric constants are observed when low-dimensional metals undergo a spin- or charge-density wave transition⁷⁴. Due to nesting of the Fermi surface, a gap Δ_0 opens in the density of states, leading to $\varepsilon \propto \Delta_0^{-2}$

on the order of 10^6 to 10^8 (Ref. 97). In general, this mechanism also holds for opening a Mott gap⁹⁶ and therefore in the following, we estimate the impact of reducing the Mott gap on ε_1 .

1. Reducing the Mott gap

Let us assume that the Mott gap is already closed, then the real part of the conductivity follows $\sigma_1(\omega) \approx A|\omega|^\beta$ at low frequency, as shown in the inset of Fig. (13), where A is a normalization factor. Any non-analytic behavior of the dielectric function $\varepsilon_1(\omega \rightarrow 0)$ can only result from a sufficiently singular form of σ_1 also at low frequency. The corresponding $\varepsilon_1(\omega)$ can directly be obtained from the Kramers-Korning relation (9), yielding

$$\varepsilon_1(\omega) = 1 + 4 \int_{-\infty}^{+\infty} \frac{\sigma_1(\omega')/\omega'}{\omega' - \omega} d\omega' \quad . \quad (11)$$

For a linear-in-frequency increase of the optical conductivity ($\beta = 1$), it is straightforward to analytically calculate $\varepsilon_1(\omega)$:

$$\varepsilon_1(\omega) = -2A \log\{\omega\} + B(\omega) \quad , \quad (12)$$

where $B(\omega)$ is an analytic function that remains finite at $\omega = 0$. Fig. (13) displays the behavior of $\varepsilon_1(\omega)$ for different values β of the power law. For $\beta = 1$, the dielectric constant $\varepsilon_1(\omega)$ assumes a logarithmic divergence at zero frequency, which is a very weak singularity. If $\beta < 1$, then $\varepsilon_1(\omega = 0)$ diverges more strongly; the static dielectric constant is just a finite number as β gets larger than unity.

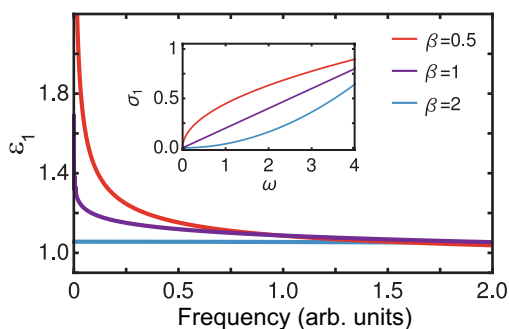


FIG. 13. Frequency dependence of the dielectric constant $\varepsilon_1(\omega)$ for different power β of the optical conductivity $\sigma_1(\omega) \propto \omega^\beta$ as plotted in the inset.

Within DMFT, the precise exponent β is still under debate⁹⁸, but it is at most of order unity, consistent with our numerical results. This means that the permittivity varies only little by reducing the Mott gap as the transition is approached from the insulating side and cannot cause the enormous dielectric enhancement found in our experiments. The latter is well described by microscopic dynamical mean-field theory combined with macroscopic

percolation theory⁹⁹. In the present case of κ -(BEDT-TTF)₂Cu₂(CN)₃, optical investigations at ambient pressure unambiguously show that no clear-cut gap exists, despite the strongly insulating behavior^{100,101}. In the THz and far-infrared range the conductivity is rather well described by a linear frequency dependence, corresponding to $\beta \approx 1$. The low-energy spectral weight actually increases upon lowering the temperature, in contrast to the quantum spin-liquid compounds κ -(BEDT-TTF)₂-Ag₂(CN)₃ and β' -EtMe₃Sb[Pd(dmit)₂]₂, which are all far away from the IMT boundary⁹. Saito *et al.* conducted low-temperature optical investigations on κ -[(BEDT-TTF)_{1-x}-(BEDT-STF)_x]₂Cu₂(CN)₃ at frequencies low enough to estimate the dielectric constant in the far-infrared range. Around 1 THz $\varepsilon_1(x)$ increases only slightly as spectral weight is transferred to low frequency as the IMT is approached by substitution¹⁰². Hence, we conclude that the observed enhancement of the permittivity upon approaching the Mott transition originates from the first-order nature and the concomitant percolating phase coexistence and is not caused by closing the Mott gap.

2. Phase coexistence at the genuine Mott transition in organic spin liquids

The enhancement of $\varepsilon_1(U/W)$ – respectively $\varepsilon_1(p)$ – is sharply confined to the coexistence region, where it exceeds the values of the (homogeneous) Mott insulator by orders of magnitude. In the related study on κ -[(BEDT-TTF)_{1-x}-(BEDT-STF)_x]₂Cu₂(CN)₃ chemical substitution was utilized to increase the bandwidth in order to tune the system across the Mott transition¹⁰². The dielectric permittivity exhibits a similar maximum when approaching the phase boundary as correlations decrease. In the coexistence regime, percolation and correlation effects both contribute to the dielectric properties. It is interesting to note that this peak appears in an abrupt fashion, very distinct to the smooth and gradual increase in disorder-driven IMT¹⁰³. Moreover, around the first-order IMT below T_{crit} , the optical conductivity exhibits a pronounced frequency dependence beyond standard percolation theory.

Finally, we draw attention to recent DMFT calculations⁹⁸ revealing a crossover (non-asymptotic) power law behavior in the spectral function $A(\omega)$ and the self-energy $-\text{Im}\{\Gamma(\omega)\}$ extending from low to elevated temperatures. Concomitantly, consistent scaling of the resistivity is found both above and below T_{crit} as well. Both are traced back to the metastable insulating phase in the coexistence region, suggesting local quantum criticality of the Mott transition below T_{crit} , which eventually is also responsible for its well-known counterpart at elevated temperatures. Besides these fundamental findings, this study reveals a peculiar low-frequency behavior of $A(\omega)$ in proximity to the Mott transition. Whether this can be connected to the intriguing dielectric response ob-

served here has yet to be clarified, but might provide a route to place the various features in $\varepsilon_1(p, T, \omega)$ on the same footing, such as the pressure evolution of the HT peak and the anomalous power-law decrease of $\varepsilon_1(\omega)$ in the coexistence region. We remind at this point that the HT peak is observed in several other organic dimer Mott insulators^{35,104,105} with triangular lattice, showing that its emergence is independent of details in the crystal structure.

3. Applicability of percolation theory

Percolation theory is applicable for systems consisting of two distinct types of domains. One should keep in mind, however, that in real materials domain walls are always present with properties distinct from either of the coexisting phases. The precise characteristics of the domain walls reflect the specifics of the clean system displaying phase coexistence and as such have particular dimensions (thickness), and as such occupy a finite volume fraction. The effects of such domain walls can be expected to be negligible if their dimension (thickness) is much smaller than the characteristic domain size, which is what we expect for weak disorder. In contrast, when disorder is sufficiently strong, it is expected^{106,107} to produce nucleation centers for more and more droplets, leading to the reduction of the domain size, which eventually becomes comparable to the thickness of the domain walls. When this happens, a simplistic two-component percolation picture is no longer of direct relevance, and one may expect more gradual variations of all observables that what is predicted by simple percolation theory. We believe finite disorder is the main reason that the peak of real part of dielectric function ε_1 appears more narrow in theoretical results than in experiments.

We want to recall that in contrast to most other examples of percolative behavior, here we do not have different materials mixed, not even the crystal structure or symmetry changes between insulating and metallic regions. In the ideal case, the domains are distinct by the effect of correlations on their physical properties. From thermal expansion studies on the related compound κ -(BEDT-TTF)₂Cu[N(CN)₂]Cl in the vicinity of the critical endpoint, we know that metallic and insulating phases exhibit a slightly different volume and distinct expansion coefficients¹⁰⁸. The particular arrangement is susceptible to strain, impurities, etc. leading to domain boundaries with an intermediate lattice constant on a local scale.

C. Phase diagram

The main results of our pressure- and temperature-dependent dielectric spectroscopic studies on κ -(BEDT-TTF)₂Cu₂(CN)₃ are summarized in Fig. 14, where a three-dimensional plot of $\varepsilon_1(p, T)$ is produced from the data taken at $f = 380$ kHz. The bottom area contains a

sketch of the phase diagram constructed on the projection of the $\varepsilon_1(p, T)$ values with the corresponding color code; the intense dark red area indicates the enhanced values in the coexistence phase when spatially separated metallic regions grow in the insulating matrix. The percolative behavior softens as temperature increases: the maximum diminishes and eventually a gradual crossover remains above T_{crit} . Additionally, we include the quantum Widom line from the data of Ref. 8 that agree with the results presented here. The bifurcation temperature T_B marks the change from the HT to the LT peak and the concomitant modification in the relaxation dynamics. The Fermi-liquid temperature T_{FL} was extracted from the resistivity $\rho_1(T)$ probed at 10 kHz as described in detail in Appendix A; our findings are in accordance with previous reports^{8,11}.

Our data provide first experimental evidence for the

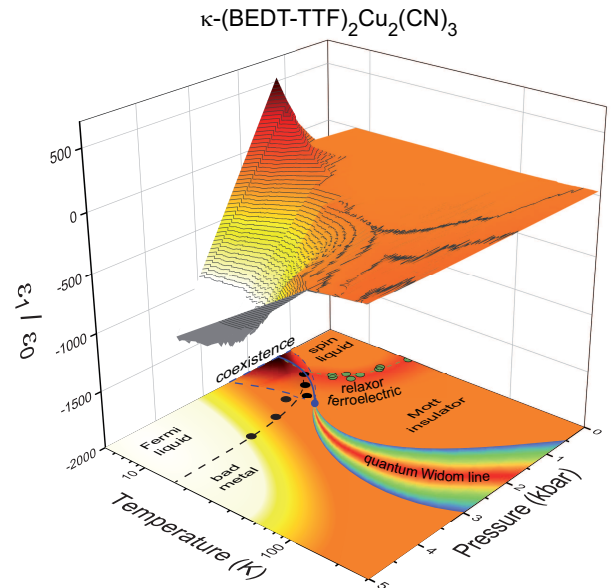


FIG. 14. 3D plot of $\varepsilon_1(p, T)$ probed at 380 kHz and the phase diagram of κ -(BEDT-TTF)₂Cu₂(CN)₃ as obtained by analyzing $\rho_1(p, T)$ at 10 kHz which is described in detail in Appendix A. Most importantly, we observe a strong increase of ε_1 up to 500, centered around 1.8 kbar and below 20 K, close to the first-order Mott transition (blue line). We ascribe this to a coexistence phase hosting spatially separated metallic and insulating regions, as predicted by dynamical mean-field theory⁴⁶. For $T > 16$ K, the first-order insulator-to-metal transition becomes a gradual crossover which is indicated by the quantum Widom line^{8,9,37}. The Mott insulating phase for $p < 1.5$ kbar reveals a relaxor ferroelectric response in $\varepsilon_1(T)$ wherein T_B (green circles) is the bifurcation temperature indicating a change in the relaxation mechanism.

coexistence of the Mott-insulating and the metallic phases, as predicted by DMFT calculations on a disordered Hubbard model for half-filling^{46,109}. This regime of metal-insulator coexistence emerges from the insulating phase and partially overlaps with the Fermi-liquid regime. When the phase boundary is crossed, the metallic fraction grows and quickly forms a continuous path through the specimen; the capacitive coupling of remaining metallic puddles in the insulating regions leads to the high values of ε_1 . The percolative behavior is strongly suppressed for higher temperatures where the first-order Mott insulator-metal transition becomes a smooth crossover and the contrast in conductivity between metallic and insulating fraction diminishes.

Approaching the phase boundary from the insulating side, we determine a critical exponent $q \approx 1$ in Eq. (5) that is consistent with Bruggeman's effective medium approximation that allowed us to extract the metallic volume filling fraction as a function of pressure.

V. SUMMARY

Our dielectric measurements as a function of frequency, temperature and pressure in the insulating state of κ -(BEDT-TTF)₂Cu₂(CN)₃ reveal that the relaxor-ferroelectric peak below $T = 50$ K shifts to lower temperatures as pressure increases because the screening by free charge carriers becomes pronounced with increasing bandwidth. A second peak emerges at lower temperatures and grows in amplitude with increasing pressure. We attribute this behavior to the sparse occurrence of metallic puddles in the insulating host phase. Upon moving deeper into the phase coexistence region of the first-order transition from the Mott insulating to the metallic phase, we discover a strong enhancement of $\varepsilon_1(p)$ up to 10^5 at lowest frequencies ($f = 7.5$ kHz), which resembles a percolating behavior. We apply Bruggeman's effective medium approximation to determine the metallic filling fraction and obtain the critical exponent $q \approx 1$ upon approaching the threshold from the insulating side. Calculations by dynamical-mean-field theory on a single-band Hubbard model reproduce our comprehensive experimental findings in full breadth. The divergency of the dielectric permittivity is mainly caused by classical percolation physics of a strongly correlated electron system close to the Mott transition. Our results provide compelling evidence for the coexistence of metallic and insulating regions, and we demonstrate the capabilities of dielectric spectroscopy as a 'smoking gun' to probe phase coexistence and spatial inhomogeneities at metal-insulator transitions.

VI. ACKNOWLEDGMENTS

We thank G. Untereiner for contacting the crystals. We acknowledge support by the Deutsche Forschungsge-

meinschaft (DFG) via DR228/52-1. E.U. acknowledges the support of the European Social Fund and by the Ministry of Science Research and the Arts of Baden-Württemberg. Work in Florida was supported by the NSF Grant No. 1822258, and the National High Magnetic Field Laboratory through the NSF Cooperative Agreement No. 1157490 and the State of Florida.

Appendix A: Resistivity curves

From the measured complex impedance we determined the out-of-plane resistivity as a function of temperature and applied pressure. Figs. 15 and 16 display the $\rho_1(T)$ curves probed at low frequency for sample 2 and sample 1, respectively. The indicated pressure values were recorded at $T = 10$ K. Although these are two-point measurements, the results are in good agreement with the four-point dc-measurements reported in literature^{8,11}, taking into account that we probe the perpendicular direction. For both samples we observe a maximum in $\rho_1(T)$ that shifts to higher T with increasing pressure; concomitantly the resistivity is reduced. The resistivity maximum at T_{\max} indicates the onset of the metallic transport regime with $d\rho_1/dT < 0$. The Fermi liquid regime is characterized by $\rho_1(T) = \rho_0 + AT^2$. We define T_{FL} as the temperature where $\rho_1(T)$ deviates by more than 10% from this quadratic behavior. We remind here, that the experimental setup did not allow for cooling below 8 K such that the superconducting state below $T_{\text{SC}} = 4$ K could not be reached.

The inset in Fig. 15(a) shows the decrease of the *in-situ* recorded pressure upon cooling. The step like features around 220 K correspond to the solidification temperature of the pressure transmitting oil. Below 50 K, the pressure saturates and becomes nearly temperature-independent. For the 0 kbar measurement, the sample was cooled in the pressure cell, which was left opened and filled with He contact gas, such that pressure loss upon cooling is negligible.

The precise in-situ measurement of $p(T)$ enables us to analyze $\rho_1(p)$ at constant temperature. In particular, we determine the quantum Widom line (QWL) by fitting $\rho_1(p)$ (orange squares) at constant temperature with $\log(\rho_{1,\text{QWL}}) = c[1 - \tanh\{b(p - p_{\text{QWL}})\}]$ (black line), as exemplarily shown in Fig. 15(d). This procedure⁹ yields the QWL as the point of inflection at p_{QWL} which is indicated by the magenta arrow.

Qualitatively, there is good agreement between both samples of completely different origin and growth conditions, whereas the IMT in sample 1 is observed at a slightly lower pressure of $p_{\text{IMT},1} = 1.05$ kbar. Consequently, also the quantum Widom line for sample 1 is slightly shifted towards lower pressures as compared to sample 2. This deviation could be attributed to a hysteresis effect, since the measurement sequence for sample 1 started with the highest pressure whereas for sample 2 with the lowest. However, it is not clear whether this re-

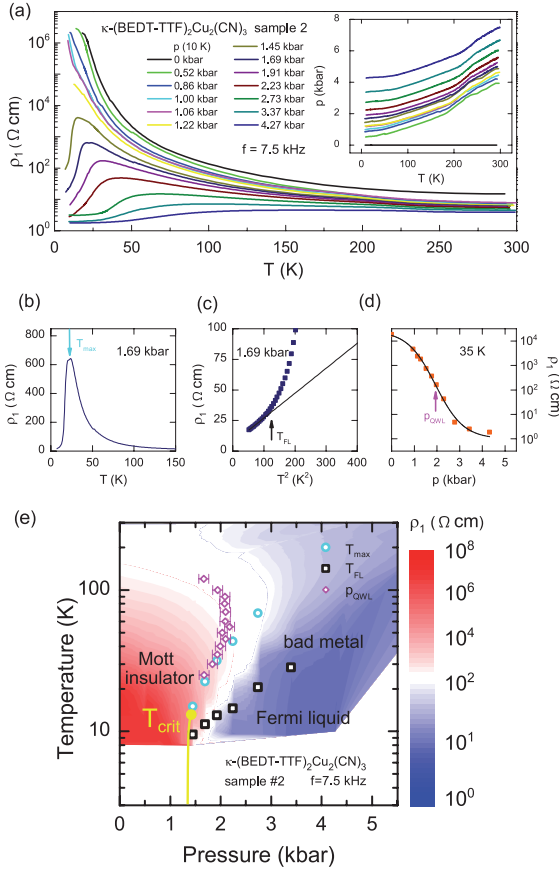


FIG. 15. (a) Temperature dependent out-of-plane resistivity $\rho_1(T)$ of κ -(BEDT-TTF) $_2$ Cu $_2$ (CN) $_3$ for sample 2 under hydrostatic pressure, measured along the a -direction and at $f = 7.5$ kHz, which is in good agreement with dc-measurements known from literature^{8,11}. With increasing pressure, $\rho_1(T)$ is reduced, revealing the insulator-metal transition for $p > 1.45$ kbar. The inset in panel (a) displays the in-situ measured pressure loss upon cooling. (b) The maximum in $\rho_1(T)$ (cyan arrow) directly indicates the onset of metallic conduction. (c) We define T_{FL} as the temperature at which ρ_1 deviates from $\rho_{1,FL} = \rho_0 + AT^2$ by more than 10%. (d) The quantum Widom line is determined by fitting $\rho_1(p)$ (orange squares) at constant temperature with $\log(\rho_{1,QWL}) = c[1 - \tanh\{b(p - p_{QWL})\}]$ (black line). (e) Phase diagram which is based on a contour plot of $\rho_1(p, T)$, including T_{max} , T_{FL} and p_{QWL} . The yellow line represents an estimate of the Mott transition with a critical end point at $T_{crit} = 16$ K and $p_{crit} = 1.45$ kbar.

ally holds here since each measurement starts at room temperature well above the IMT. Therefore, it might also indicate an enhanced degree of structural disorder in sample 1. Such a sample dependence is confirmed by disorder studies on the sister compound κ -(BEDT-TTF) $_2$ Cu[N(CN) $_2$]Cl, which reveal a shift of p_{IMT} to lower pressures upon x-ray irradiation¹¹⁰.

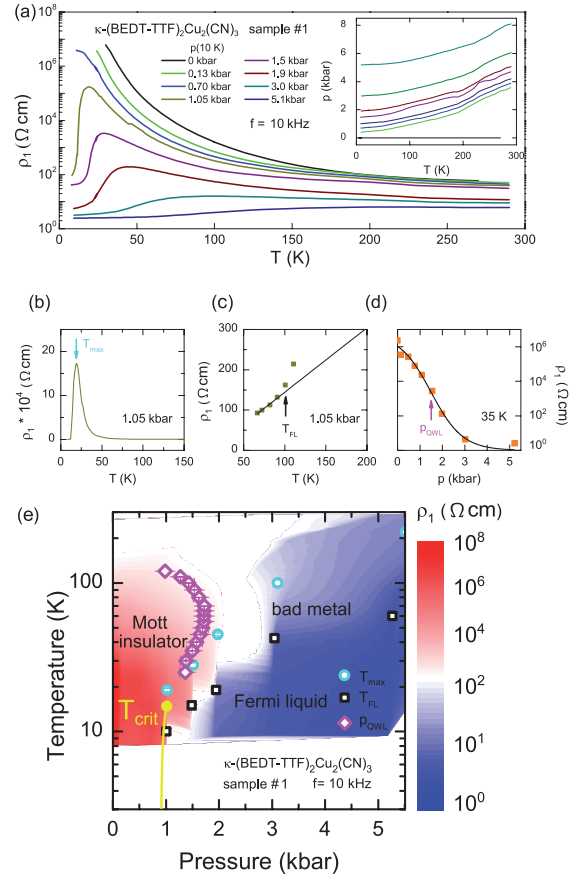


FIG. 16. Temperature dependent resistivity $\rho_1(T)$ of κ -(BEDT-TTF) $_2$ Cu $_2$ (CN) $_3$ sample 1 under hydrostatic pressure measured at $f = 10$ kHz in the direction perpendicular to the bc -plane. The panels correspond to those of sample 2, presented in Fig. 15.

Appendix B: Dielectric properties of sample 1

Most data presented above have been obtained from dielectric measurements on sample 2; the conclusions on the phase separation at the Mott IMT are fully supported by similar finding on sample 1. Fig. 17 gives an overview on the pressure evolution of its dielectric response by plotting $\varepsilon_1(T)$ for selected frequencies and pressures as indicated. The position of the HT feature at ambient pressure, for instance at 40 K when probed at $f = 100$ kHz, is in good agreement with previous ambient pressure reports^{25,26}. Unfortunately, only a few measurements in the Mott insulating phase could be performed before the sample broke. Nevertheless, despite the low pressure resolution, it is obvious that the shift of the HT peak upon increasing pressure resembles the findings for sample 2. In contrast, the LT peak for sample 1 is barely visible up to $p = 0.45$ kbar and becomes evident only at 0.7 kbar around $T = 10$ K. The strong enhancement of ε_1 by several orders of magnitude upon entering the coexistence regime is already observed at $p = 1.0$ kbar and extends up to 1.9 kbar [Fig. 17(f)]. We emphasize

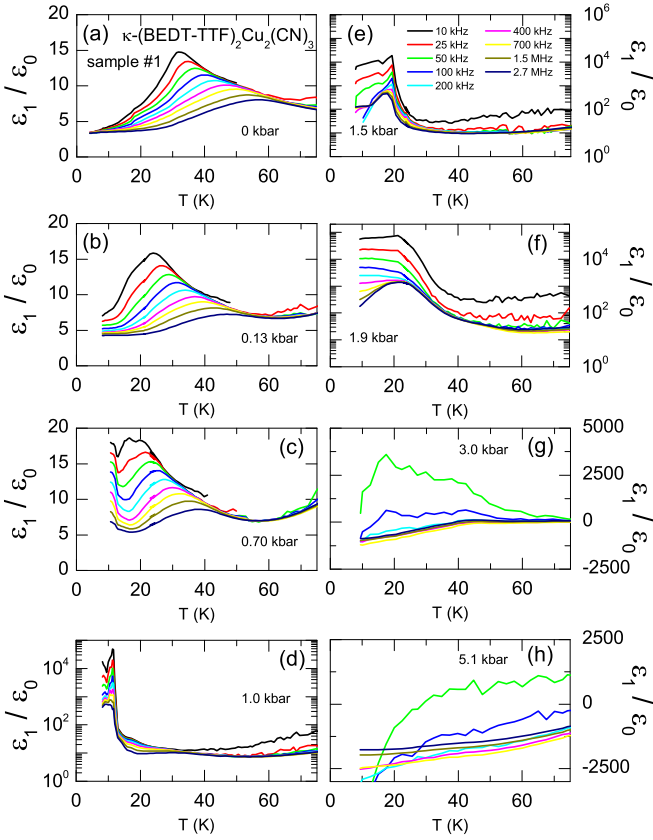


FIG. 17. Plot of the dielectric permittivity $\varepsilon_1(T)$ of κ -(BEDT-TTF) $_2$ Cu $_2$ (CN) $_3$ sample 1 for several frequencies upon increasing pressure. The results are qualitatively identical to the one obtained of sample 2, displayed in Fig. 1. (a) At ambient pressure the relaxor-type ferroelectric peak starts already around $T = 70$ K and reaches the maximum at low frequencies at 30 K. (b-c) A shoulder-like feature is already present at ambient pressure and develops into a second peak upon pressurizing. (d-f) In the coexistence phase between $p = 1.0$ and 1.9 kbar, an enormous increase of ε_1 is observed due to percolation. (g,h) Above $p = 3.0$ kbar, $\varepsilon_1 < 0$ for nearly all measured frequencies indicating metallic behavior.

that this is in accordance with the shift of the IMT in sample 1. Interestingly, the plateau-like shape of $\varepsilon_1(T)$ is observed only for $f \leq 400$ kHz whereas for higher frequencies a slight downturn occurs. Upon further pressure increase, metallic behavior with $\varepsilon_1 < 0$ sets in whereas only for the lowest frequencies positive values for the permittivity remain.

In order to analyze the frequency-dependent permittivity of these data, we have applied same the procedure as presented above on sample 2. The obtained fit parameters $\Delta\varepsilon^{\text{mode } 1}$, $1 - \alpha_1$ and τ_1 for mode 1 are plotted in Fig. 18 as a function of inverse temperature. The peak in $\Delta\varepsilon^{\text{mode } 1}(T)$ shifts to lower T and increases in amplitude as pressure is applied. This behavior is reminiscent to what is observed for sample 2, however, it is less pronounced for sample 1, for which the LT peak is weaker

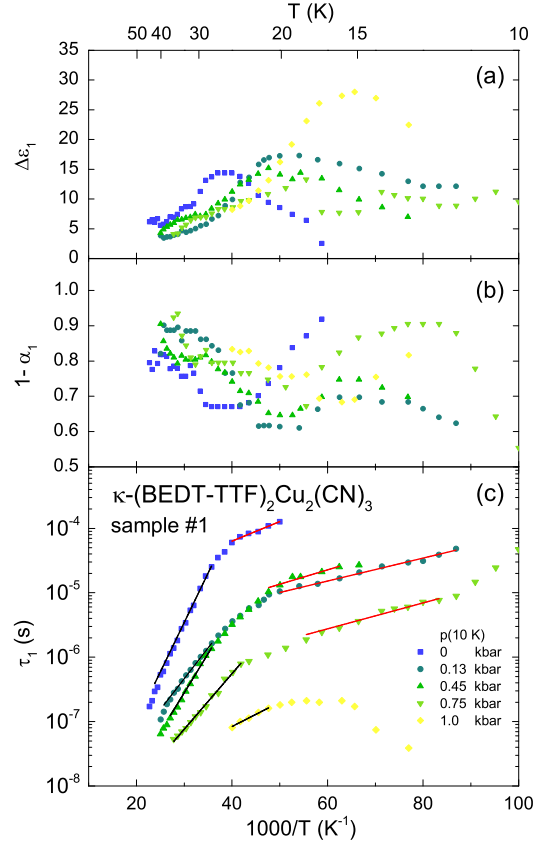


FIG. 18. Arrhenius plot of the fitting parameters of mode 1 for sample 1 at different pressures as indicated. (a) Dielectric strength $\Delta\varepsilon^{\text{mode } 1}(T)$, (b) distribution of relaxation times $1 - \alpha_1(T)$ and (c) mean relaxation time $\tau_1(T)$. The black and red lines represent fits with Eq. (3) above and below the kink in $\tau_1(T)$ at T_B , respectively.

and becomes apparent only at $p \geq 1.0$ kbar. This also explains the higher values of $1 - \alpha_1$ and their restrengthening upon cooling, the latter most pronounced at ambient pressure, which indicate less broadening in sample 1. In $\tau_1(T)$, a kink at T_B is observed, which shifts to lower temperatures while the corresponding relaxation time gets shorter, reproducing the behavior observed in the previous sample. The parameters obtained by fitting $\tau_1(T)$ with the activated behavior [Eq. (3)] for the HT mode ($T > T_B$) and the LT mode ($T < T_B$) are already presented and discussed above in Fig. 6.

Fig. 19 displays the parameters $\Delta\varepsilon^{\text{mode } 2}(T)$, $1 - \alpha_2(T)$ and $\tau_2(T)$ of mode 2 for sample 1 of κ -(BEDT-TTF) $_2$ Cu $_2$ (CN) $_3$. The dielectric strength $\Delta\varepsilon^{\text{mode } 2}$ exhibits a maximum around $T = 30$ K at ambient pressure, which shifts towards lower temperatures and diminishes upon increasing p . This is in contrast to sample 2, for which $\Delta\varepsilon^{\text{mode } 2}$ monotonously grows upon cooling (cf. Fig. 7). Throughout the whole pressure range $\Delta\varepsilon^{\text{mode } 2}$ is smaller than the one of mode 1 by approximately a factor of 2. The mode shifts towards lower temperatures with rising pressure. A drop in $1 - \alpha_2(T)$ indicates a consid-

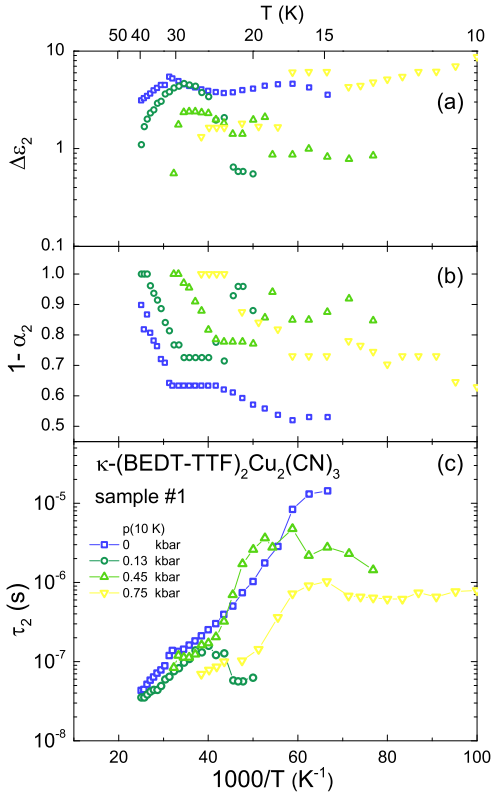


FIG. 19. Arrhenius plot of the fit parameters of mode 2 for κ -(BEDT-TTF) $_2$ Cu $_2$ (CN) $_3$ sample 1 at different pressures as indicated. (a) Dielectric strength $\Delta\epsilon_2^{\text{mode } 2}(T)$, (b) distribution of relaxation times $1 - \alpha_2(T)$, and (c) mean relaxation time $\tau_2(T)$.

erable broadening of the mode upon cooling, which gets less pronounced for increasing pressure. The temperature dependence of τ_2 is strongly influenced by pressure and sample dependent. For sample 1, the monotonic increase is much steeper and observed down to 15 K at ambient pressure which saturates into a plateau upon increasing pressure. In contrast to sample 2, only the onset of a shallow minimum around $T = 12$ K is revealed indicating non-monotonic relaxation dynamics.

Appendix C: Spurious effects

1. Contacts

Owing to the two-point configuration usually applied in dielectric spectroscopy, the obtained data may include contributions from polarization effects at the contacts, which have to be conscientiously ruled out or determined. At elevated temperatures, the samples exhibit semi-conducting transport properties (cf. Figs.15 and 16). Since the contacts are produced by amorphous carbon (carbon paste) with metallic properties, Schottky contacts may form at the sample-contact interfaces, re-

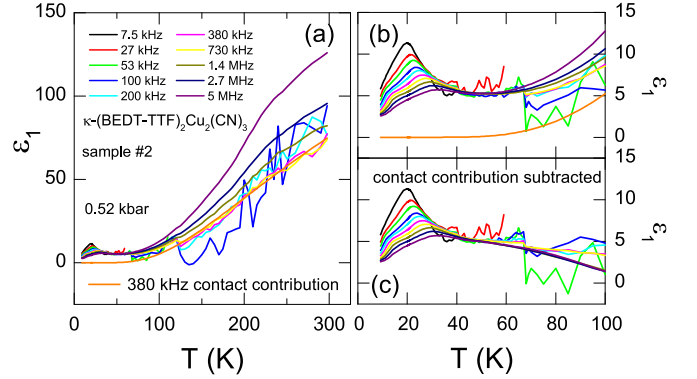


FIG. 20. (a) Temperature dependence of $\epsilon_1(T)$ plotted in the entire temperature range, for an applied pressure of $p = 0.52$ kbar measured at various frequencies f . In addition, we determine the contact contribution by fitting the high-temperature part with Eq. (C2), as shown for the example of $f = 380$ kHz (orange line). (b) Detailed view of the relaxor ferroelectric relaxation at low temperatures including the contact contribution. (c) Relaxor ferroelectric response after the contact contribution has been subtracted: the contact contribution is negligible below $T = 60$ K.

sulting in a depletion layer at the interface with thickness

$$d_{\text{depl}} = \left(\frac{2\epsilon_1\epsilon_0}{eN_c} (\Phi_m - \Phi_s \pm eU) \right)^{1/2}, \quad (\text{C1})$$

wherein Φ_m and Φ_s the distances between the vacuum level and the chemical potential of the metal and semiconductor, respectively, and U indicates the voltage of the applied ac signal. The charge carrier density $N_c(T) \propto \exp\{-\Delta/k_B T\}$ is determined by thermal excitations across the charge gap Δ . The modified charge density in the depletion zone gives rise to the an additional capacitance

$$C_{\text{depl}} \propto \frac{1}{d_n} \propto C \exp\left\{ \frac{-\Delta}{2k_B T} \right\}, \quad (\text{C2})$$

which eventually is responsible for the spurious effects attributed to the contact contribution. In the right side of Eq. (C2) we estimated the temperature dependence of the contact contribution, which is governed by $N_c(T)$. In Fig. 20(a) we exemplarily plot $\epsilon_1(T)$ up to room temperature and probed at various frequencies as indicated. In the temperature range $75 \text{ K} < T < 300 \text{ K}$, we observe a decrease of $\epsilon_1(T)$ upon cooling which is very well described by Eq. (C2) (orange line) and hence is attributed to the contact contribution.

Most importantly, the contact contribution is negligible below 60 K [Fig. 20(b)] and does not influence the analysis of the relaxor like dielectric response [Fig. 20(c)]. We also note, that this effect would be too weak to explain the huge enhancement of $\epsilon_1(T)$ close to the phase boundary. If we have a look at $\rho_1(T)$ and $\epsilon_1(T)$ at 1.91 kbar, for instance, we find that $\rho_1(p = 1.91 \text{ kbar}, T = 10 \text{ K}) \approx \rho_1(p = 1.91 \text{ kbar}, T = 300 \text{ K})$,

such that the spurious contact contribution to ε_1 should be the same at 10 K and 300 K. On the other hand, we see that $\varepsilon_1(p = 1.91 \text{ kbar}, T = 10 \text{ K}) \gg \varepsilon_1(p =$

$1.91 \text{ kbar}, T = 300 \text{ K})$ (cf. Fig. 1), which can not be explained by solely considering the contacts, corroborating our phase coexistence scenario.

-
- ¹ H. Seo, C. Hotta, and H. Fukuyama, *Chem. Rev.* **104**, 5005 (2004).
- ² A. Lebed, ed., *The physics of organic superconductors and conductors*, Springer Series in Materials Science, Vol. 110 (Springer-Verlag, Berlin, 2008).
- ³ B. J. Powell and R. H. McKenzie, *Rep. Prog. Phys.* **74**, 56501 (2011).
- ⁴ T. Ishiguro, K. Yamaji, and G. Saito, *Organic superconductors*, 2nd ed. (Springer-Verlag, Berlin, 1998); N. Toyota, M. Lang, and J. Müller, *Low-Dimensional Molecular Metals*, Springer Series in Solid-State Sciences, Vol. 154 (Springer-Verlag, Berlin, 2007); T. Mori, *Electronic Properties of Organic Conductors* (Springer, Tokyo, 2016).
- ⁵ S. Lefebvre, P. Wzietek, S. Brown, C. Bourbonnais, D. Jérôme, C. Mézière, M. Fourmigué, and P. Batail, *Phys. Rev. Lett.* **85**, 5420 (2000).
- ⁶ P. Limelette, P. Wzietek, S. Florens, A. Georges, T. A. Costi, C. Pasquier, D. Jérôme, C. Mézière, and P. Batail, *Phys. Rev. Lett.* **91**, 016401 (2003).
- ⁷ F. Kagawa, K. Miyagawa, and K. Kanoda, *Nature* **436**, 534 (2005); *Nat. Phys.* **5**, 880 (2009).
- ⁸ T. Furukawa, K. Miyagawa, H. Taniguchi, R. Kato, and K. Kanoda, *Nat. Phys.* **11**, 221 (2015); T. Furukawa, K. Kobashi, Y. Kurosaki, K. Miyagawa, and K. Kanoda, *Nat. Comm.* **9**, 307 (2018).
- ⁹ A. Pustogow, M. Bories, A. Löhle, R. Rösslhuber, E. Zhukova, B. Gorshunov, S. Tomić, J. A. Schlueter, R. Hübner, T. Hiramatsu, Y. Yoshida, G. Saito, R. Kato, T.-H. Lee, V. Dobrosavljević, S. Fratini, and M. Dressel, *Nat. Mat.* **17** (2018).
- ¹⁰ H. Terletska, J. Vučićević, D. Tanasković, and V. Dobrosavljević, *Phys. Rev. Lett.* **107**, 026401 (2011); J. Vučićević, D. Tanasković, M. J. Rozenberg, and V. Dobrosavljević, *Phys. Rev. Lett.* **114**, 246402 (2015).
- ¹¹ Y. Shimizu, K. Miyagawa, K. Kanoda, M. Maesato, and G. Saito, *Phys. Rev. Lett.* **91**, 107001 (2003); Y. Kurosaki, Y. Shimizu, K. Miyagawa, K. Kanoda, and G. Saito, *Phys. Rev. Lett.* **95**, 177001 (2005).
- ¹² K. Kanoda and R. Kato, *Annu. Rev. Condens. Matter Phys.* **2**, 167 (2011).
- ¹³ L. Savary and L. Balents, *Rep. Prog. Phys.* **80**, 016502 (2017).
- ¹⁴ Y. Zhou, K. Kanoda, and T.-K. Ng, *Rev. Mod. Phys.* **89**, 025003 (2017).
- ¹⁵ M. Dressel and A. Pustogow, *J. Phys.: Condens. Matter* **30**, 203001 (2018); A. Pustogow, Y. Saito, E. Zhukova, B. Gorshunov, R. Kato, T.-H. Lee, S. Fratini, V. Dobrosavljević, and M. Dressel, *Phys. Rev. Lett.* **121**, 056402 (2018).
- ¹⁶ M. Dressel, P. Lazić, A. Pustogow, E. Zhukova, B. Gorshunov, J. A. Schlueter, O. Milat, B. Gumhalter, and S. Tomić, *Phys. Rev. B* **93**, 081201 (2016).
- ¹⁷ J.-P. Pouget, P. Alemany, and E. Canadell, *Mater. Horiz.* **5**, 590 (2018).
- ¹⁸ P. Foury-Leykian, V. Ilakovac, V. Balédent, P. Fertey, A. Arakcheeva, O. Milat, D. Petermann, G. Guillier, K. Miyagawa, K. Kanoda, P. Alemany, E. Canadell, S. Tomić, and J.-P. Pouget, *Crystals* **8** (2018).
- ¹⁹ R. S. Manna, M. de Souza, A. Brühl, J. A. Schlueter, and M. Lang, *Phys. Rev. Lett.* **104**, 016403 (2010); R. S. Manna, S. Hartmann, E. Gati, J. A. Schlueter, M. de Souza, and M. Lang, *Crystals* **8** (2018).
- ²⁰ S. Yamashita, Y. Nakazawa, M. Oguni, Y. Oshima, H. Nojiri, Y. Shimizu, K. Miyagawa, and K. Kanoda, *Nat. Phys.* **4**, 459 (2008).
- ²¹ M. Yamashita, N. Nakata, Y. Kasahara, T. Sasaki, N. Yoneyama, N. Kobayashi, S. Fujimoto, T. Shibauchi, and Y. Matsuda, *Nat. Phys.* **5**, 44 (2009).
- ²² M. Poirier, M. de Lafontaine, K. Miyagawa, K. Kanoda, and Y. Shimizu, *Phys. Rev. B* **89**, 045138 (2014).
- ²³ T. Isono, T. Terashima, K. Miyagawa, K. Kanoda, and S. Uji, *Nat. Comm.* **7** (2016).
- ²⁴ M. Poirier, S. Parent, A. Côté, K. Miyagawa, K. Kanoda, and Y. Shimizu, *Phys. Rev. B* **85**, 134444 (2012).
- ²⁵ M. Abdel-Jawad, I. Terasaki, T. Sasaki, N. Yoneyama, N. Kobayashi, Y. Uesu, and C. Hotta, *Phys. Rev. B* **82**, 125119 (2010).
- ²⁶ M. Pinterić, M. Čulo, O. Milat, M. Basletić, B. Korin-Hamzić, E. Tafra, A. Hamzić, T. Ivek, T. Peterseim, K. Miyagawa, K. Kanoda, J. A. Schlueter, M. Dressel, and S. Tomić, *Phys. Rev. B* **90**, 195139 (2014); M. Pinterić, T. Ivek, M. Čulo, O. Milat, M. Basletić, B. Korin-Hamzić, E. Tafra, A. Hamzić, M. Dressel, and S. Tomić, *Physica B* **460**, 202 (2015); M. Pinterić, D. Rivas Góngora, Z. Rapljenović, T. Ivek, M. Čulo, B. Korin-Hamzić, O. Milat, B. Gumhalter, P. Lazić, M. Sanz Alonso, W. Li, A. Pustogow, G. Gorgen Lesseux, M. Dressel, and S. Tomić, *Crystals* **8** (2018).
- ²⁷ C. Hotta, *Phys. Rev. B* **82**, 241104 (2010); *Crystals* **2**, 1155 (2012).
- ²⁸ M. Naka and S. Ishihara, *J. Phys. Soc. Jpn.* **79**, 063707 (2010).
- ²⁹ H. Li, R. T. Clay, and S. Mazumdar, *J. Phys.: Condens. Matter* **22**, 272201 (2010); S. Dayal, R. T. Clay, H. Li, and S. Mazumdar, *Phys. Rev. B* **83**, 245106 (2011); R. T. Clay, S. Dayal, H. Li, and S. Mazumdar, *phys. stat. sol. (b)* **249**, 991 (2012).
- ³⁰ H. Gomi, M. Ikenaga, Y. Hiragi, D. Segawa, A. Takahashi, T. J. Inagaki, and M. Aihara, *Phys. Rev. B* **87**, 195126 (2013).
- ³¹ Y. Shimizu, K. Miyagawa, K. Kanoda, M. Maesato, and G. Saito, *Phys. Rev. B* **73**, 140407 (2006).
- ³² K. Sedlmeier, S. Elsässer, D. Neubauer, R. Beyer, D. Wu, T. Ivek, S. Tomić, J. A. Schlueter, and M. Dressel, *Phys. Rev. B* **86**, 245103 (2012).
- ³³ K. Yakushi, K. Yamamoto, T. Yamamoto, Y. Saito, and A. Kawamoto, *J. Phys. Soc. Jpn.* **84**, 084711 (2015).
- ³⁴ S. Tomić and M. Dressel, *Rep. Prog. Phys.* **78**, 096501 (2015).
- ³⁵ M. Pinterić, P. Lazić, A. Pustogow, T. Ivek, M. Kuveždić, O. Milat, B. Gumhalter, M. Basletić, M. Čulo, B. Korin-Hamzić, A. Löhle, R. Hübner, M. Sanz Alonso, T. Hira-

- matsu, Y. Yoshida, G. Saito, M. Dressel, and S. Tomić, Phys. Rev. B **94**, 161105 (2016).
- ³⁶ P. Lazić, M. Pinterić, D. Rivas Góngora, A. Pustogow, K. Treptow, T. Ivek, O. Milat, B. Gumhalter, N. Došlić, M. Dressel, and S. Tomić, Phys. Rev. B **97**, 245134 (2018).
- ³⁷ U. Geiser, H. H. Wang, K. D. Carlson, J. M. Williams, H. A. Charlier, J. E. Heindl, G. A. Yaconi, B. J. Love, M. W. Lathrop, J. E. Schirber, D. Overmyer, J. Ren, and M.-H. Whangbo, Inorg. Chem. **30**, 2586 (1991).
- ³⁸ T. Komatsu, N. Matsukawa, T. Inoue, and G. Saito, J. Phy. Soc. Jpn. **65**, 1340 (1996).
- ³⁹ *Impedance measurement handbook*, Keysight technologies, 6th ed. (2009).
- ⁴⁰ R. Rösslhuber, E. Uykur, and M. Dressel, Rev. Sci. Instr. **89**, 054708 (2018).
- ⁴¹ S. Sasaki, S. Iguchi, N. Yoneyama, and T. Sasaki, J. Phy. Soc. Jpn. **84**, 074709 (2015).
- ⁴² L. E. Cross, “Relaxor ferroelectrics,” in *Piezoelectricity: Evolution and Future of a Technology* (Springer-Verlag, Berlin, Heidelberg, 2008) pp. 131–155.
- ⁴³ D. Staresinić, K. Biljaković, P. Lunkenheimer, and A. Loidl, Solid State Commun. **137**, 241 (2006).
- ⁴⁴ Y. E. Ryabov, A. Puzenko, and Y. Feldman, Phys. Rev. B **69**, 014204 (2004).
- ⁴⁵ A. Georges, G. Kotliar, W. Krauth, and M. J. Rozenberg, Rev. Mod. Phys. **68**, 13 (1996).
- ⁴⁶ J. Vučićević, H. Terletska, D. Tanasković, and V. Dobrosavljević, Phys. Rev. B **88**, 075143 (2013).
- ⁴⁷ D. Stroud, Phys. Rev. B **12**, 3368 (1975); D. Stroud and F. P. Pan, Phys. Rev. B **17**, 1602 (1978).
- ⁴⁸ S. Kirkpatrick, Rev. Mod. Phys. **45**, 574 (1973).
- ⁴⁹ T. C. Choy, *Effective Medium Theory: Principles and Applications*, 2nd ed. (Oxford University Press, Oxford, 2015).
- ⁵⁰ B. I. Shklovskii and A. L. Efros, *Electronic Properties of Doped Semiconductors* (Springer-Verlag, Berlin, 1984).
- ⁵¹ A. L. Efros and B. I. Shklovskii, phys. stat. sol. (b) **76**, 475 (1976).
- ⁵² L. Benguigui, J. Phys. Lett. (Paris) **46**, L (1985).
- ⁵³ J. P. Clerc, G. Giraud, J. M. Laugier, and J. M. Luck, Adv. Phys. **39**, 191 (1990).
- ⁵⁴ M. Hövel, B. Gompf, and M. Dressel, Phys. Rev. B **81**, 035402 (2010); Thin Solid Films **519**, 2955 (2011).
- ⁵⁵ R. B. Laibowitz and Y. Gefen, Phys. Rev. Lett. **53**, 380 (1984).
- ⁵⁶ M. F. Hundley and A. Zettl, Phys. Rev. B **38**, 10290 (1988).
- ⁵⁷ C. S. Yoon and S.-I. Lee, Phys. Rev. B **42**, 4594 (1990).
- ⁵⁸ A. B. Pakhomov, S. K. Wong, X. Yan, and X. X. Zhang, Phys. Rev. B **58**, R13375 (1998).
- ⁵⁹ A. K. Sarychev and F. Brouers, Phys. Rev. Lett. **73**, 2895 (1994).
- ⁶⁰ E. Economou, *Green’s Functions in Quantum Physics*, 3rd ed. (Springer-Verlag, Berlin, 2006).
- ⁶¹ B. M. Letfulov and J. K. Freericks, Phys. Rev. B **64**, 174409 (2001), 10.1103/PhysRevB.64.174409.
- ⁶² H. Fukuyama, J.-i. Kishine, and M. Ogata, J. Phy. Soc. Jpn. **86**, 123706 (2017).
- ⁶³ I. Voloshenko, F. Kuhl, B. Gompf, A. Polity, G. Schoening, A. Berrier, and M. Dressel, Appl. Phys. Lett. **113**, 201906 (2018); I. Voloshenko, B. Gompf, A. Berrier, G. Schoening, F. Kuhl, A. Polity, and M. Dressel, J. Vac. Sci. Technol. B **37**, 061202 (2019).
- ⁶⁴ P. Lunkenheimer, J. Müller, S. Krohns, F. Schrettle, A. Loidl, B. Hartmann, R. Rommel, M. de Souza, C. Hotta, J. Schlueter, and M. Lang, Nat. Mater. **11**, 755 (2012).
- ⁶⁵ S. Tomić, M. Pinterić, T. Ivek, K. Sedlmeier, R. Beyer, D. Wu, J. A. Schlueter, D. Schweitzer, and M. Dressel, J. Phys.: Condens. Matter **25**, 436004 (2013).
- ⁶⁶ M. M. Qazilbash, M. Brehm, B.-G. Chae, P.-C. Ho, G. O. Andreev, B.-J. Kim, S. J. Yun, A. V. Balatsky, M. B. Maple, F. Keilmann, H.-T. Kim, and D. N. Basov, Science **318**, 1750 (2007).
- ⁶⁷ T. Sasaki, N. Yoneyama, N. Kobayashi, Y. Ikemoto, and H. Kimura, Phys. Rev. Lett. **92**, 227001 (2004).
- ⁶⁸ N. Mott, *Metal-Insulator Transitions*, 2nd ed. (Taylor & Francis, 1990).
- ⁶⁹ H. v. Löhneysen, “The metal-insulator transition in Si:P,” in *Festkörperprobleme 30*, edited by U. Rössler (Springer-Verlag, Berlin, Heidelberg, 1990) pp. 95–111; in *Advances in Solid State Physics Vol. 40*, edited by B. Kramer (Springer, Berlin, 2000) pp. 143–167; Annalen der Physik **523**, 599 (2011).
- ⁷⁰ F. Evers and A. D. Mirlin, Rev. Mod. Phys. **80**, 1355 (2008).
- ⁷¹ E. Abrahams, ed., *50 years of Anderson localization* (World Scientific Publishing Co., Singapore, 2010).
- ⁷² D. Stauffer and A. Aharony, *Introduction to Percolation Theory*, 2nd ed. (CRC Press, Boca Raton, Florida, 1994).
- ⁷³ B. Bollobás and O. Riordan, *Percolation* (Cambridge University Press, Cambridge, 2006).
- ⁷⁴ G. Grüner, *Density Waves in Solids* (Addison-Wesley, Reading, MA, 1994).
- ⁷⁵ P. Monceau, Adv. Phys. **61**, 325 (2012).
- ⁷⁶ F. Gebhard, *The Mott Metal-Insulator Transition* (Springer-Verlag, Berlin, Heidelberg, 1997).
- ⁷⁷ M. Imada, A. Fujimori, and Y. Tokura, Rev. Mod. Phys. **70**, 1039 (1998).
- ⁷⁸ P. P. Edwards, C. N. R. Rao, and N. Mott, *Metal-insulator transitions revisited* (Taylor & Francis, London, 1995).
- ⁷⁹ V. E. Dubrov, M. E. Levinshstein, and M. S. Shur, Sov. Phys. JETP **43**, 1050 (1976).
- ⁸⁰ D. J. Bergman and Y. Imry, Phys. Rev. Lett. **39**, 1222 (1977); D. J. Bergman, Phys. Rep. **43**, 377 (1978).
- ⁸¹ L. Genzel and U. Kreibig, Z. Physik B **37**, 93 (1980).
- ⁸² T. G. Castner, N. K. Lee, G. S. Cieloszyk, and G. L. Salinger, Phys. Rev. Lett. **34**, 1627 (1975); T. G. Castner, Phys. Rev. B **20**, 3505 (1979).
- ⁸³ T. F. Rosenbaum, R. F. Milligan, M. A. Paalanen, G. A. Thomas, R. N. Bhatt, and W. Lin, Phys. Rev. B **27**, 7509 (1983).
- ⁸⁴ M. Hering, M. Scheffler, M. Dressel, and H. v. Löhneysen, Phys. Rev. B **75**, 205203 (2007).
- ⁸⁵ D. M. Grannan, J. C. Garland, and D. B. Tanner, Phys. Rev. Lett. **46**, 375 (1981).
- ⁸⁶ M. A. van Dijk, G. Casteleijn, J. G. H. Joosten, and Y. K. Levine, J. Chem. Phys. **85**, 626 (1986).
- ⁸⁷ M. T. Clarkson and S. I. Smedley, Phys. Rev. A **37**, 2070 (1988); M. T. Clarkson, Phys. Rev. A **37**, 2079 (1988).
- ⁸⁸ Y. Alexandrov, N. Kozlovich, Y. Feldman, and J. Texter, J. Chem. Phys. **111**, 7023 (1999).
- ⁸⁹ C. Pecharromán and J. S. Moya, Adv. Mater. **12**, 294 (2000); C. Pecharromán, F. Esteban-Betegón, J. F. Bartolomé, S. López-Esteban, and J. S. Moya, **13**, 1541 (2001).

- ⁹⁰ C.-W. Nan, Y. Shen, and J. Ma, *Ann. Rev. Mater. Res.* **40**, 131 (2010).
- ⁹¹ S. Berthier, J. Peiro, S. Fagnent, and P. Gadenne, *Physica A* **241**, 1 (1997).
- ⁹² S. De Zuani, T. Peterseim, A. Berrier, B. Gompf, and M. Dressel, *Applied Physics Letters* **104**, 241109 (2014); S. De Zuani, M. Rommel, B. Gompf, A. Berrier, J. Weis, and M. Dressel, *ACS Photonics* **3**, 1109 (2016).
- ⁹³ F. Pan, D. Stroud, and D. Tanner, *Solid State Commun.* **20**, 271 (1976).
- ⁹⁴ M. M. Qazilbash, A. Tripathi, A. A. Schafgans, B.-J. Kim, H.-T. Kim, Z. Cai, M. V. Holt, J. M. Maser, F. Keilmann, O. G. Shpyrko, and D. N. Basov, *Phys. Rev. B* **83**, 165108 (2011); T. J. Huffman, D. J. Lahneman, S. L. Wang, T. Slusar, B.-J. Kim, H.-T. Kim, and M. M. Qazilbash, *Phys. Rev. B* **97**, 085146 (2018).
- ⁹⁵ P. Limelette, A. Georges, D. Jérôme, P. Wzietek, P. Metcalf, and J. M. Honig, *Science* **302**, 89 (2003).
- ⁹⁶ C. Aebischer, D. Baeriswyl, and R. M. Noack, *Phys. Rev. Lett.* **86**, 468 (2001).
- ⁹⁷ M. Dressel and G. Grüner, *Electrodynamics of solids* (Cambridge University Press, Cambridge, 2002).
- ⁹⁸ H. Eisenlohr, S.-S. B. Lee, and M. Vojta, *Phys. Rev. B* **100**, 155152 (2019).
- ⁹⁹ A. Pustogow, R. Rösslhuber, Y. Tan, E. Uykur, A. Böhme, A. Löhle, R. Hübner, J. A. Schlueter, M. Dressel, and V. Dobrosavljević, arXiv:1907.04437 (2019).
- ¹⁰⁰ I. Kézsmárki, Y. Shimizu, G. Mihály, Y. Tokura, K. Kanoda, and G. Saito, *Phys. Rev. B* **74**, 201101 (2006).
- ¹⁰¹ K. Sedlmeier, S. Elsässer, D. Neubauer, R. Beyer, D. Wu, T. Ivek, S. Tomić, J. A. Schlueter, and M. Dressel, *Phys. Rev. B* **86**, 245103 (2012).
- ¹⁰² Y. Saito, R. Rösslhuber, A. Löhle, M. Sanz Alonso, M. Wenzel, A. Kawamoto, A. Pustogow, and M. Dressel, ArXiv:1911.06766.
- ¹⁰³ J. C. Dyre and T. B. Schrøder, *Rev. Mod. Phys.* **72**, 873 (2000).
- ¹⁰⁴ M. Abdel-Jawad, N. Tajima, R. Kato, and I. Terasaki, *Phys. Rev. B* **88**, 075139 (2013).
- ¹⁰⁵ S. Iguchi, S. Sasaki, N. Yoneyama, H. Taniguchi, T. Nishizaki, and T. Sasaki, *Phys. Rev. B* **87**, 075107 (2013).
- ¹⁰⁶ Y. Imry and S.-k. Ma, *Phys. Rev. Lett.* **35**, 1399 (1975).
- ¹⁰⁷ V. Dobrosavljević, N. Trivedi, and J. M. Valles, Jr., eds., *Conductor Insulator Quantum Phase Transitions* (Oxford University Press, Oxford, 2012).
- ¹⁰⁸ E. Gati, M. Garst, R. S. Manna, U. Tutsch, B. Wolf, L. Bartosch, H. Schubert, T. Sasaki, J. A. Schlueter, and M. Lang, *Sci. Adv.* **2**, e1601646 (2016).
- ¹⁰⁹ K. Byczuk, W. Hofstetter, and D. Vollhardt, *Phys. Rev. Lett.* **94**, 056404 (2005).
- ¹¹⁰ E. Gati, U. Tutsch, A. Naji, M. Garst, S. Khler, H. Schubert, T. Sasaki, and M. Lang, *Crystals* **8** (2018).